Estimating charge-transport properties of fuel-cell and electrolyzer catalyst layers via electrochemical impedance spectroscopy*

A. Kosakian[a,b], M. Secanell[a,*]

[a] *Energy Systems Design Laboratory, Department of Mechanical Engineering, University of Alberta, Canada*
[b] *Department of Mathematical and Statistical Sciences, University of Alberta, Canada*

Abstract

Electrochemical impedance spectroscopy is the most common experimental technique for measuring the charge-transport properties of catalyst layers. Such a measurement relies on fitting the impedance spectrum with analytical impedance expressions. To date, a study that examines the suitability of the available analytical models for such analysis does not exist. In this work, a numerical one-dimensional catalyst-layer model is used to assess the validity of the analytical models for estimating catalyst-layer charge-transport properties. An ohmic-heating-based approach to computing ohmic resistance is used to examine the relationship between conductivity, resistance, and impedance of various catalyst layers representative of those used in proton-exchange-membrane fuel cells and water electrolyzers. The ohmic-heating analysis indicates that the most commonly used impedance expressions (Eikerling and Kornyshev, 1999; Makharia et al., 2005) result in a threefold overestimation of protonic resistance and may not be applicable to the proton-conductivity estimation for electrolyzer catalyst layers that exhibit low electronic conductivity. A more recent analytical model (Kulikovsky, 2017) is shown to produce protonic- and electronic-transport properties that agree with numerical simulations. The results of this work are used to provide recommendations for the selection of analytical impedance expressions for a given operating regime (H_2/O_2 or H_2/N_2) and an observed shape of the measured spectrum in order to achieve an accurate charge-transport characterization of a catalyst layer. A novel graphical approach to analyzing H_2/N_2 spectra is also proposed. Although the considered analytical models are not applicable to heterogeneous catalyst layers and no general algebraic conductivity-resistance relationship exists in that case, it is shown that the H_2/N_2 impedance measurement of heterogeneous catalyst layers provides the total ohmic resistance. A two-dimensional fuel-cell model is used to show that the anode catalyst layer may cause a distortion of the impedance spectrum at frequencies above 5 Hz that obstructs the charge-transport characterization with analytical models.

Keywords: fuel cell, water electrolyzer, catalyst layer, electrochemical impedance spectroscopy, charge transport

1. Introduction

One of the main roles of catalyst layers (CLs) in hydrogen-fueled proton-exchange-membrane fuel cells (PEMFCs) and water electrolyzers (PEMWEs) is the transport of protons and electrons to and from the reaction sites. Catalyst

*This is the authors' preprint of the article published in Electrochimica Acta on November 23, 2020 (`https://doi.org/10.1016/j.electacta.2020.137521`). This document does not contain the corrections and improvements made during the review and proof processes. Please cite the published article.

*Corresponding author
Email address: `secanell@ualberta.ca` (M. Secanell)

layers used in both PEMFC electrodes and in PEMWE cathodes are typically made of a carbon-supported catalyst (platinum or a platinum-based alloy)[1–7] and a perfluorosulfonic-acid-based ionomer, such as Nafion®[8,9]. Effective protonic conductivity of such layers has been shown to be up to four orders of magnitude lower than electronic conductivity[10–12] and to affect reaction distribution (and hence catalyst utilization)[13] and overall performance[13–15] of PEMFC CLs. Therefore, measuring the protonic conductivity of those layers is an important part of the design and development of fuel cells and electrolyzers. In contrast, the anode catalyst layers (ACLs) of PEMWEs are usually made of iridium dioxide (unsupported[3,6], supported on titanium dioxide[4,5,16] or on titanium[7]) and Nafion®. These layers do not exhibit the high electronic conductivity[4,7,17] observed in carbon-based CLs, and, therefore, estimation of both protonic and electronic conductivities of PEMWE anodes is essential.

Electrochemical impedance spectroscopy (EIS) is the primary method used to measure the proton-transport properties of fuel-cell catalyst layers[10,12,18–46] and was also recently used to estimate the protonic resistance of PEMWE ACLs under H_2/N_2 conditions[16,47]. A vital part of these measurements is fitting the experimental spectra with analytical impedance expressions, such as those derived by Eikerling and Kornyshev[48] and by Makharia et al.[19] These expressions, however, are only valid for small operating current and when the electronic resistance of the catalyst layer is negligible[19,48]. Therefore, the use of these relations in the analysis of PEMWE ACLs must be carefully assessed. More recently, Kulikovsky[49] derived a generalized analytical low-current impedance expression that takes the finite electronic conductivity of the CL into account. The relationship between ohmic resistance and effective conductivity predicted by that model[49],

$$R_\Omega = \frac{L}{3\sigma^{\text{eff}}},$$

is thrice lower than in the earlier models[19,48],

$$R_\Omega = \frac{L}{\sigma^{\text{eff}}}.$$

Thus, consistency of the models from references[19,48] and[49] must be examined.

To date, a study that compares the available impedance expressions and conclusively assesses the validity of the resistance-conductivity relationships proposed in references[19,48,49] with an independent (non-EIS-based) technique does not exist. The analytical expressions[19,48,49] are also based on a simplified Tafel kinetic model, and the impact on the impedance spectrum of the changing Tafel slope in a more appropriate multi-step kinetic model, such as that for oxygen reduction in PEMFCs[50–52], has not been investigated.

Another critical assumption used in the models from references[19,48,49] is catalyst-layer homogeneity. Recent tomography data suggest that catalyst layers may have nonuniform spatial distribution of catalyst, support, and ionomer[53,54]. Such heterogeneity has been hypothesized[20–22,38,55–58] to cause distortion in the high-frequency 45° impedance branch in the Nyquist representation[16,21,34,38,47,56–64] that is used to estimate the charge-transport properties of catalyst layers. Correlation of conductivity, ohmic resistance, and impedance of such layers remains an open question.

Analytical models[19,48,49] were derived for a single catalyst layer and ignore the effect of other cell components. Charge-transport analysis of fuel-cell impedance spectra may be obstructed by the appearance of an additional capacitive arc at high frequencies[62,65–67] (typically above 1 kHz[62,65,66]). This arc has been hypothesized to represent faradaic processes in the anode[66,67]. On the other hand, it has been claimed to disappear in H_2/H_2 measurements[68],

which suggests its cathodic nature. Therefore, better understanding of the physical phenomena behind the additional arc at frequencies above 1 kHz needs to be developed.

The aim of this work is to examine the validity of the previously proposed methods [19,48,49] for estimating the catalyst-layer charge-transport properties from H_2/O_2 and H_2/N_2 spectra and to study the relationship between conductivity and ohmic resistance in case of homogeneous and heterogeneous catalyst layers of PEMFCs and PEMWEs. For this purpose, a numerical 1D catalyst layer model is used that allows for an unambiguous correlation of impedance, resistance, and conductivity through the ohmic-heating based approach proposed [69,70] and validated [62] earlier by the authors. Various pairs of electronic and protonic conductivities and different protonic-conductivity distributions are used to develop valuable insight for different electrochemical systems and catalyst-layer compositions. The effect of the reaction kinetics on the impedance spectrum is also investigated using the double-trap kinetic model for the oxygen-reduction reaction (ORR) on platinum [50–52]. The previously developed transient 2D PEMFC model [62] is used to analyze the effect of the anode catalyst layer on fuel-cell impedance.

2. Numerical model

2.1. Catalyst-layer model

2.1.1. Assumptions

The transient two-dimensional PEMFC model published earlier [62] was reduced to a one-dimensional model of a catalyst layer. The simplifying assumptions, additional to those listed in reference [62], are given below:

1. the ionomer phase of the catalyst layer was assumed to have a constant and uniform conductivity;
2. transport of water in the layer was neglected;
3. the model is isothermal; temperature was assumed constant and uniform;
4. a macrohomogeneous catalyst-layer model was used [71].

Assumptions 1–3 were used in order to analyze the catalyst-layer impedance in isolation from other cell components and dynamic processes, such as electrolyte hydration and heat generation. The assumptions listed above allow for a direct comparison of the numerical model to the analytical expressions, which rely on similar simplifications.

2.1.2. Governing equations

The model describes transport of oxygen, protons, and electrons in a cathode catalyst layer (CCL) of a PEMFC via the following set of governing equations:

$$\varepsilon_{\mathrm{v}} c_{\mathrm{tot}} \frac{\partial x_{\mathrm{O_2}}}{\partial t} - \nabla \cdot \left(c_{\mathrm{tot}} D_{\mathrm{O_2}}^{\mathrm{eff}} \nabla x_{\mathrm{O_2}} \right) = -\frac{j}{4F}, \tag{1}$$

$$-C_{\mathrm{dl}} \frac{\partial \eta}{\partial t} - \nabla \cdot \left(\sigma_{\mathrm{H^+}}^{\mathrm{eff}} \nabla \phi_{\mathrm{H^+}} \right) = -j, \tag{2}$$

$$C_{\mathrm{dl}} \frac{\partial \eta}{\partial t} - \nabla \cdot \left(\sigma_{\mathrm{e^-}}^{\mathrm{eff}} \nabla \phi_{\mathrm{e^-}} \right) = j, \tag{3}$$

where $\eta = \phi_{\mathrm{e^-}} - \phi_{\mathrm{H^+}} - E_{\mathrm{th}}$ is the overpotential and E_{th} is the theoretical half-cell potential. The equations above are given in a multidimensional form since the model considered in this work is a derivative of the earlier developed 2D PEMFC model [62] and is inherently multi-dimensional. The single spatial dimensionality was achieved by reducing

Table 1: Boundary conditions in the CL model (Γ denotes a domain boundary).

Solution variable	CL-PEM	CL-PTL	Symmetry
x_{O_2}	no flux	$x_{O_2}(t, \Gamma) = x^0_{O_2}$	no flux
ϕ_{H^+}	$\phi_{H^+}(t, \Gamma) = 0$	no flux	no flux
ϕ_{e^-}	no flux	$\phi_{e^-}(t, \Gamma) = V(t)$	no flux

the in-plane domain size to 0.1 µm. When reduced to equations (2) and (3), the model also represents a PEMWE anode catalyst layer operating under H_2/N_2 conditions (i.e., fed with nitrogen).

To retain consistency with analytical models[19,48,49], the volumetric faradaic current density in equations (1)–(3) was computed using Tafel kinetics:

$$j = i_0 A_v \left(\frac{c^{cat|i}_{O_2}}{c^{ref}_{O_2}} \right)^{\gamma} \exp\left(-\frac{\alpha F \eta}{RT} \right), \tag{4}$$

where $c^{ref}_{O_2}$ is the reference oxygen concentration (mol/cm^3), $c^{cat|i}_{O_2}$ is the oxygen concentration at the catalyst-ionomer interface (mol/cm^3) computed using Henry's law, γ is the reaction order with respect to oxygen concentration, and α is the charge-transfer coefficient.

The numerical model (1)–(3) also supports the computation of the faradaic current density from the double-trap kinetic model for oxygen-reduction-reaction (ORR) on platinum[50–52]:

$$j = 2j^* \theta_{OH} \exp\left(-\frac{\Delta G^*_{RD}}{kT} \right) - 2j^* \theta_{Pt} \exp\left(-\frac{\Delta G^*_{\text{-RD}}}{kT} \right), \tag{5}$$

where j^* is a reference prefactor (A/cm^3), θ_i is the coverage of the platinum surface with species i, ΔG^*_{RD} and $\Delta G^*_{\text{-RD}}$ denote the potential-dependent free energy of activation (eV) for the forward and backward reductive-desorption steps in the ORR, respectively, and k is the Boltzmann constant (eV/K). Equations (4) and (5) are shown in this work to produce the same catalyst-layer impedance at high frequencies, confirming that it is independent of the charge-transfer resistance.

2.1.3. Initial and boundary conditions

The initial solution for the transient problem given in equations (1)–(3) was obtained by first solving the governing equations at steady state and then importing the resulting solution into the transient simulation at $t = 0$. Boundary conditions listed in Table 1 reflect the fact that the anode, the proton-exchange membrane (PEM), and the porous transport layer (PTL; consists of a microporous and a gas-diffusion layer in PEMFCs) are not considered in the CL model. The bulk oxygen molar fraction $x^0_{O_2}$ was computed with the ideal gas law for the given operating conditions as discussed in reference[71]. The EIS simulations were performed by applying a time-dependent voltage $V(t)$ at the CL-PTL interface.

2.1.4. Input parameters

Model parameters and operating conditions are listed in Table 2. The majority of the parameters were taken from reference[62], except for the kinetic parameters for the Tafel equation (4). The selected kinetic parameters for the Tafel model were obtained by fitting the high operating current density in a Tafel plot, where a doubled Tafel slope was observed[72,73]. When the double-trap model (5) was used, the kinetic parameters were taken to be the

Table 2: Input parameters for the CL model.

Parameter	**Value/expression**	**Details**
Operating temperature T, K	353.15	Ref.[62]
Operating pressure, atm	1.5	Ref.[62]
Relative humidity	0.5	Ref.[62]
Bulk molar fraction of oxygen prior to humidification	0.21 (H_2/O_2EIS), 10^{-10} (H_2/N_2 EIS)	Assumed
Catalyst-layer thickness, µm	4.5	Ref.[62]
Catalyst-layer porosity, ε_v	0.53	Ref.[62]
Effective oxygen diffusivity $D^{\text{eff}}_{O_2}$, cm^2/s	0.0185[a]	Ref.[62]
Effective proton conductivity $\sigma^{\text{eff}}_{H^+}$, S/cm	Table 3	Varied
Effective electron conductivity $\sigma^{\text{eff}}_{e^-}$, S/cm	Table 3	Varied
Volumetric double-layer capacitance, F/cm^3	54	Ref.[62]
Henry's law constant for oxygen in Nafion® $H_{O_2,N}$, $Pa\,cm^3/mol$	$3.1664 \cdot 10^{10}$	Ref.[74]
Reference oxygen concentration $c^{\text{ref}}_{O_2}$, mol/cm^3	$5 \cdot 101325/H_{O_2,N}$	Ref.[72]
Exchange current density i_0, A/cm^2_{cat}	$3.08 \cdot 10^{-6} \exp\left(-\frac{28920.95}{R}\left(\frac{1}{T}-\frac{1}{323.15}\right)\right)$	Ref.[75 b]
Active area A_v, cm^2_{cat}/cm^3	212,000	Ref.[62]
Oxygen reaction order γ	1	Ref.[73,75]
Charge-transfer coefficient α	0.5	Ref.[75]

[a] Includes Knudsen effects as discussed in reference[62].

[b] The exchange-current-density equation was fitted by Moore et al.[75] to the experimental data from Parthasarathy et al.[72] with different values of the reference temperature and the pre-exponential factor. Those experimental data, however, do not match those in another publication by Parthasarathy et al.[73]. The equation for i_0 shown here produces the exchange current density between the experimental values found in references[72,73].

same as in reference[62]. The layer properties given in Table 2 correspond to an inkjet-printed catalyst layer with platinum loading of about 0.15 mg/cm^2 and Nafion® loading of 30 wt% and were either measured experimentally or computed for the given operating conditions as discussed in reference[62].

Protonic- and electronic-conductivity values were varied in order to investigate the effect of charge transport in both conductive phases of homogeneous fuel-cell and electrolyzer CLs on the impedance spectrum. Case I in Table 3 corresponds to the effective charge-transport properties computed for this layer in reference[62]. The reference protonic conductivity in case I corresponds to the average absorbed-water content of 4 $mol_{H_2O}/mol_{SO_3^-}$ in a vapor-equilibrated CL at 50% RH. Since electrolyte-hydration effects were neglected, the same protonic conductivity was used at all current densities considered in this work, thus allowing for an unambiguous attribution of the impedance-spectrum changes to the varied current distribution in the layer rather than to the complex hydration effects. Twice lower protonic conductivity was used in case II to highlight its effect on the length of the linear high-frequency feature in the catalyst-layer impedance spectrum. Cases III and IV were designed to illustrate the shape of the spectrum when the conductivity of both conductive phases is either high or low, respectively. Protonic- and electronic-conductivity values were swapped in case V, mirroring case I. As it will be shown in this work, swapping conductivities does not affect the catalyst-layer impedance spectrum. Therefore, analysis of the spectra simulated with the parameters from Table 3 reflects not only PEMFC CLs and PEMWE CCLs ($\sigma^{\text{eff}}_{e^-} > \sigma^{\text{eff}}_{H^+}$), but also PEMWE ACLs ($\sigma^{\text{eff}}_{e^-} \lessapprox \sigma^{\text{eff}}_{H^+}$, swapped cases I–IV).

Table 3: The homogeneous-CCL model parameters varied between the considered cases.

Case	$\sigma^{\mathrm{eff}}_{\mathrm{H^+}}$, mS/cm	$\sigma^{\mathrm{eff}}_{\mathrm{e^-}}$, mS/cm
I	2.00	3788
II	1.00	3788
III	2000	3788
IV	2.00	37.9
V	3788	2.00

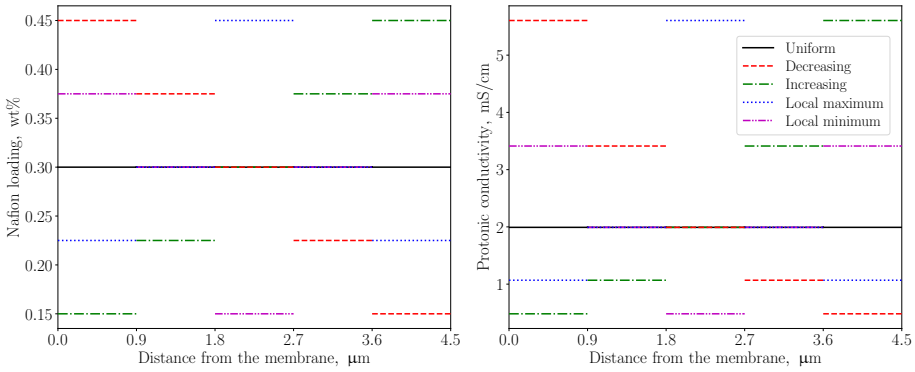

Figure 1: Illustration of the heterogeneous-catalyst-layer property distributions used in this work: a) ionomer loading; and b) effective protonic conductivity. The resulting ionomer-to-carbon weight ratio and ionomer volume fraction varied from 0.29 to 1.4 and from 0.07 to 0.33, respectively. The "decreasing", "increasing", and "uniform" distributions coincide at $x \in [1.8, 2.7)$ μm; the "local maximum", "local minimum", and "uniform" distributions coincide at $x \in [0.9, 1.8) \cup [2.7, 3.6)$ μm.

The effect of catalyst layer heterogeneity on the impedance spectrum was analyzed by varying the ionomer distribution along the CL thickness. Continuous conductivity distributions have been commonly considered in the impedance-modeling literature, such as exponential[55,63,76,77] and linear[21] distributions and a distribution with an inflection point[78]. A graded catalyst layer was considered in this work with five through-plane zones, each 0.9-μm-thick and containing a different amount of ionomer. Such a catalyst layer can be fabricated, for instance, using inkjet printing (see, for instance, references[3,31,32] for the description of the method). The ionomer-loading distributions and the corresponding effective protonic conductivities are given in Figure 1, where the uniform distribution corresponds to case I. The transport properties of the layer were computed with the relations provided in reference[62] to automatically account for structural variations. The electronic conductivity remained the same as in case I (the volume fraction of the electronically conductive phase was about 0.30 in all cases). Porosity varied between 0.37 and 0.63, which translated into an effective diffusivity that was about 2 times lower and 1.4 times higher than in the reference case.

2.1.5. Solution approach and post-processing

The transient catalyst-layer model was implemented in the open-source, in-house fuel-cell modeling software OpenFCST[79,80] based on the finite-element library deal.II[81,82]. The implicit Euler method was used for the temporal

discretization, and the time-step size was automatically adjusted by Richardson extrapolation[83,84] with the relative solution-error tolerance of 10^{-3}. The finite-element method with the second-order Lagrange shape functions was used for the spatial discretization that resulted in a problem with 1,935 and 6,939 degrees of freedom depending on the input parameters. Newton's method with the relative solution-error tolerance of 10^{-4} was used to linearize the problem. The numerical accuracy of the solution was ensured by performing mesh-independence and time-step-size studies.

The H_2/O_2 impedance spectra were computed by simulating a current-density response to a fast, 1-ns-long linear ramp of 1 mV in voltage followed by a 10^4–10^6-s long voltage hold (typically several orders of magnitude longer than required to achieve a new steady state). The initial and final voltages were chosen such that the respective current densities were within 1% of the target operating value. The details about this method can be found in references[62,85], where this rapid-EIS approach was shown to be equivalent to the conventional sine-wave approach to EIS. The time-step size was gradually increased from the initial value of 10^{-10} s by 1% between the time layers, which was found sufficient in terms of the numerical accuracy of the resulting spectra. Each impedance spectrum was computed as the ratio of non-equispaced Fourier transforms[86] of the voltage and current-density signals for 2,000 logarithmically spaced frequencies between 10^{-6} and 10^7 Hz.

To simulate the H_2/N_2 spectra, the oxygen molar fraction at the boundary with the gas-diffusion layer was reduced to 10^{-10} and the steady-state voltage was set to 0.9 V. The resulting current density was of the order of 10^{-12} A/cm^2 and was considered sufficiently small to approximate the oxygen-free operation. The rapid-EIS approach was found inefficient in this case, as the time-step size was severely restricted by the Richardson-extrapolation algorithm. Instead, the H_2/N_2 spectra were computed by simulating sinusoidal voltage waves at 134 frequencies between 1 and 10^7 Hz with the peak-to-peak amplitude of 1 mV. At each frequency, 5 wave periods were generated and resolved with 1024 points per period for numerical accuracy. The current-density response, scaled with the Welch window function[87] to minimize aliasing, was processed with the Fast Fourier Transform (FFT) from SciPy[88]. Impedance was then computed as the ratio of the known voltage phasor to the reconstructed current-density phasor.

Ohmic resistance was computed in the numerical model through ohmic heating[62,69,70] (in $\Omega \cdot \mathrm{cm}^2$):

$$R^{\mathrm{eff}}_{\mathrm{H^+}} = \frac{1}{i^2 A} \int \sigma^{\mathrm{eff}}_{\mathrm{H^+}} \nabla\phi_{\mathrm{H^+}} \cdot \nabla\phi_{\mathrm{H^+}}\, dV, \tag{6}$$

$$R^{\mathrm{eff}}_{\mathrm{e^-}} = \frac{1}{i^2 A} \int \sigma^{\mathrm{eff}}_{\mathrm{e^-}} \nabla\phi_{\mathrm{e^-}} \cdot \nabla\phi_{\mathrm{e^-}}\, dV, \tag{7}$$

where A is the in-plane area of the catalyst layer and V is its volume.

All simulations were performed using a single thread of an Intel® Xeon® E5-2690 v2 CPU at 3.00 GHz. The simulation time varied between 1 and 21 h depending on the chosen EIS approach and the input parameters. Each polarization curve took approximately 20–25 s of computational time.

2.2. Fuel-cell model

The previously published transient two-dimensional PEMFC model[62] was used with no changes except for the following two simplifications:

1. microporous layers were not included in the model;
2. catalyst layers were assumed to be macrohomogeneous[71].

The listed assumptions were made to reduce the computational time and had no effect on the generality of the impedance analysis presented in this work. All input parameters were taken the same as in reference [71] (353.15 K, 1.5 atm, 50% RH, pure-oxygen supply in the cathode). Spatial discretization with the finite-element method and the second-order Lagrange shape functions resulted in a problem with 54,390 degrees of freedom. Impedance spectra were simulated using the rapid-EIS approach [62,85] with the time-stepping algorithm discussed in this work. Computational time varied in the presented parametric studies between 11 and 36 hours using five threads of an Intel® Xeon® E5-2690 v2 CPU at 3.00 GHz.

3. Analytical models for homogeneous catalyst layers

The analytical expressions for the H_2/O_2 and H_2/N_2 impedance considered in this section were derived from 1D catalyst-layer models, similar to the one given by equations (1)–(3), under the assumption of the catalyst-layer homogeneity [19,48,49]. The main differences between the models by Eikerling and Kornyshev [48] (and Makharia et al. [19]) and by Kulikovsky [49] is the transmission-line representation of the catalyst layer and the neglect of the electronic resistance in the former work. The analytical impedance relations from references [19,48,49], as well as their assumptions and limiting cases, are discussed in detail in this section.

Since the models considered here are for catalyst layers only, they cannot be applied directly to analyze experimental impedance spectra. In the PEMFC and PEMWE EIS experiments, resistance of the membrane, the porous transport layers, the bipolar plates, and contact resistance are a part of the measured real impedance at all frequencies. If those resistances are known, they should be subtracted from the real impedance to obtain a spectrum that is representative of a catalyst layer. Such a correction is only valid under H_2/N_2 and low-current H_2/O_2 conditions (when the effects of other cell components, such as membrane hydration and gas transport in PTLs, are minimized) and when the reference-electrode effects are negligible (those are discussed later in this work). Ohmic resistance of cell components can be measured independently (see references [89–93]), though contact resistance is difficult to estimate, as it may vary between cell assemblies. Unless stated otherwise, the EIS analysis presented in this work is performed for catalyst-layer impedance.

3.1. H_2/O_2 spectroscopy

3.1.1. Estimation of proton-transport properties

The first equation describing impedance of an electrode pore is attributed to de Levie [94]. It was obtained from a transmission-line representation of a pore and is given (in Ω) by [94]

$$Z_{\text{pore}} = \sqrt{Z_{\text{int}} R_{\text{pore}}} \coth\left(L_{\text{pore}} \sqrt{\frac{R_{\text{pore}}}{Z_{\text{int}}}} \right), \tag{8}$$

where Z_{int} is the interfacial impedance in $\Omega \cdot \text{cm}$, R is the ohmic resistance of the pore in Ω/cm, and L is the pore length in cm.

Eikerling and Kornyshev [48] considered a transmission-line representation of a cathode catalyst layer shown in Figure 2 and derived expressions of the form similar to equation (8) for various operating regimes of a fuel cell. For the H_2/O_2 operation at small current and under the assumptions of the catalyst-layer homogeneity and the negligible

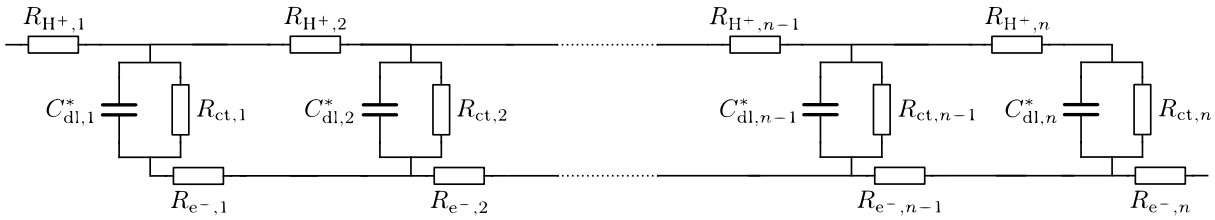

Figure 2: Transmission-line representation of a catalyst layer. The circuit is connected to the membrane at the left end and to the microporous/gas-diffusion layer at the right end. Oxygen-transport limitations are neglected.

electronic resistance (the latter is a fair simplification for the carbon-supported catalyst layers), they found [48]

$$Z = \sqrt{R_{\mathrm{H}^+,i} Z_{\mathrm{int},i}} \coth\left(\sqrt{\frac{R_{\mathrm{H}^+,i}}{Z_{\mathrm{int},i}}} \frac{L}{L_{\mathrm{e}}}\right), \tag{9}$$

where

$$Z_{\mathrm{int},i} = \frac{R_{\mathrm{ct},i}}{1 + \mathrm{i}\omega R_{\mathrm{ct},i} C^*_{\mathrm{dl},i}}, \tag{10}$$

L and L_{e} are the thickness of the catalyst layer and the length of each link in the transmission line, respectively, $R_{\mathrm{ct},i}$ and $R_{\mathrm{ct},i}$ are in $\Omega \cdot \mathrm{cm}^2$, and $C^*_{\mathrm{dl},i}$ is in $\mathrm{F/cm}^2$.

Equation (9) is given in terms of the elementary resistances and capacitances of the circuit (the common index i is used to emphasize the assumption of homogeneity) and cannot be applied directly to analyze the measured impedance spectra. Makharia et al. [19] rearranged equation (9) to obtain the impedance relation involving the macroscopic properties of the catalyst layer:

$$Z^{\mathrm{EKM}} = \sqrt{R^{\mathrm{EKM}}_{\mathrm{H}^+} Z^{\mathrm{EKM}}_{\mathrm{int}}} \coth\left(\sqrt{\frac{R^{\mathrm{EKM}}_{\mathrm{H}^+}}{Z^{\mathrm{EKM}}_{\mathrm{int}}}}\right), \tag{11}$$

where

$$Z^{\mathrm{EKM}}_{\mathrm{int}} = \frac{R^{\mathrm{EKM}}_{\mathrm{ct}}}{1 + \mathrm{i}\omega R_{\mathrm{ct}^{\mathrm{EKM}}} C^{*\,\mathrm{EKM}}_{\mathrm{dl}}}, \tag{12}$$

$$R^{\mathrm{EKM}}_{\mathrm{H}^+} = R_{\mathrm{H}^+,i} \frac{L}{L_{\mathrm{e}}}, \quad R^{\mathrm{EKM}}_{\mathrm{ct}} = R_{\mathrm{ct},i} \frac{L_{\mathrm{e}}}{L}, \quad C^{*\,\mathrm{EKM}}_{\mathrm{dl}} = C^*_{\mathrm{dl},i} \frac{L}{L_{\mathrm{e}}}. \tag{13}$$

The "EKM" superscript (Eikerling-Kornyshev-Makharia) is used here to distinguish this result from the rest of the results discussed in this work. Impedance (11) can be derived directly from the governing equations (1)–(3); an example derivation for the simple 1D case with fast oxygen and electron transport is given in Appendix A. This analytical model has been used in the literature to estimate the catalyst-layer protonic resistance of low-temperature PEMFCs [19,20] and high-temperature PEMFCs [41].

Ratio L/L_{e} gives the number of the links considered in the transmission-line representation of the catalyst layer. Because it was assumed in reference [48] that the elementary protonic resistance is related to the macroscopic protonic conductivity through $R_{\mathrm{H}^+,i} = L_{\mathrm{e}}/\sigma^{\mathrm{eff}}_{\mathrm{H}^+}$, equation (13) suggests that the macroscopic protonic resistance is

$$R^{\mathrm{EKM}}_{\mathrm{H}^+} = \frac{L}{\sigma^{\mathrm{eff}}_{\mathrm{H}^+}}. \tag{14}$$

At high frequencies, equation (11) is transformed into [48]

$$Z^{\mathrm{EKM}} = \omega^{-1/2} \sqrt{\frac{R^{\mathrm{EKM}}_{\mathrm{H}^+}}{C^{*\,\mathrm{EKM}}_{\mathrm{dl}}}} \frac{\sqrt{2}}{2} (1 - \mathrm{i}). \tag{15}$$

Unlike equation (11), equation (15) is not restricted to small current [48]. Because the real and the negative imaginary parts of equation (15) are equal, it predicts a linear 45° branch in the spectrum. It is convenient to rewrite equation (15) as

$$\left|Z^{\mathrm{EKM}}\right| = \omega^{-1/2}\sqrt{\frac{R_{\mathrm{H^+}}^{\mathrm{EKM}}}{C_{\mathrm{dl}}^{*\,\mathrm{EKM}}}}. \tag{16}$$

When the double-layer capacitance is known (for instance, from an independent measurement, such as cyclic voltammetry), equation (16) provides a simple way to extract $R_{\mathrm{H^+}}^{\mathrm{EKM}}$ from the slope of the experimental impedance magnitude plotted against $\omega^{-1/2}$. Equation (16) has been used to measure the catalyst-layer proton-transport properties of PEMFCs [18,36] and direct-methanol fuel cells (DMFCs) [43,44].

Eikerling and Kornyshev [48] provided some alternative forms of equation (11) that account for oxygen transport but are limited to either fast proton transport or negligible spatial gradients in the potential and oxygen distributions in the catalyst layer. Cruz-Manzo and Chen [95] generalized the impedance equation (11) by using constant-phase elements ($Z_{\mathrm{CPE}} = \left(Q(\mathrm{i}\omega)^{\beta}\right)^{-1}$, $\beta \in [0,\,1]$) instead of capacitors ($Z_{\mathrm{C}} = (\mathrm{i}\omega C)^{-1}$) to account for non-uniform charge distribution in the catalyst layer due to an electrochemical reaction. They also considered oxygen transport in their model; however, it does not directly affect the high-frequency spectrum (an indirect effect could occur through the electrolyte hydration, which was not modeled).

3.1.2. Simultaneous estimation of proton- and electron-transport properties

Kulikovsky [49] derived a more general expression (compared to equation (11)) for a 1D catalyst-layer impedance that accounts for the transport of protons, electrons, and oxygen (in $\Omega \cdot \mathrm{cm}^2$):

$$Z^{\mathrm{K}} = Z_{\mathrm{ct+pe}}^{\mathrm{K}} + Z_{\mathrm{ox}}^{\mathrm{K}}, \tag{17}$$

where

$$Z_{\mathrm{ct+pe}}^{\mathrm{K}} = \frac{L}{\sigma_{\mathrm{H^+}}^{\mathrm{eff}}}\frac{\mathrm{i}q\sin(p) + (1+\mathrm{i})\left(2k_\sigma + \left(1+k_\sigma^2\right)\cos(p)\right)}{k_\sigma\left(\mathrm{i}q - (1+\mathrm{i})p\right)\sin(p)}, \tag{18}$$

$$Z_{\mathrm{ox}}^{\mathrm{K}} = \frac{b(1-W)}{i\left(W - \frac{\omega^2}{\omega_{\mathrm{ct}}\omega_0} + \mathrm{i}\omega\left(\frac{1}{\omega_{\mathrm{ct}}} + \frac{1}{\omega_0}\right)\right)\left(1 + \frac{\mathrm{i}\omega}{\omega_{\mathrm{ct}}}\right)},$$

$$p = \sqrt{-\left(\hat{i} + \mathrm{i}\hat{\Omega}\right)\left(1 + \frac{1}{k_\sigma}\right)},$$

$$q = \sqrt{2k_\sigma\left(1+k_\sigma\right)\left(\mathrm{i}\hat{i} - \hat{\Omega}\right)},$$

$$k_\sigma = \frac{\sigma_{\mathrm{e^-}}^{\mathrm{eff}}}{\sigma_{\mathrm{H^+}}^{\mathrm{eff}}}, \quad \hat{i} = \frac{iL}{\sigma_{\mathrm{H^+}}^{\mathrm{eff}}b}, \quad \hat{\Omega} = \frac{\omega C_{\mathrm{dl}}L^2}{\sigma_{\mathrm{H^+}}^{\mathrm{eff}}},$$

$$W = \frac{\tanh\left(\sqrt{\left(i + \mathrm{i}4Fc^0L\omega\right)/i_{\mathrm{ox}}}\right)}{\sqrt{\left(i + \mathrm{i}4Fc^0L\omega\right)/i_{\mathrm{ox}}}},$$

$$\omega_0 = \frac{i}{4Fc^0L}, \quad \omega_{\mathrm{ct}} = \frac{i}{C_{\mathrm{dl}}bL}, \quad i_{\mathrm{ox}} = \frac{4FD_{\mathrm{O_2}}^{\mathrm{eff}}c^0}{L},$$

i is the operating current density ($\mathrm{A/cm^2}$), $b = RT/(\alpha F)$ is the Tafel slope (V), and c^0 is the oxygen concentration at the CL-PTL interface ($\mathrm{mol/cm^3}$; corresponds to $x_{\mathrm{O_2}}^0$ in Table 1). Here, $Z_{\mathrm{ct+pe}}$ is the impedance due to charge-transfer and charge-transport processes taking place in the catalyst layer and Z_{ox} is the impedance due to oxygen

transport. Equation (17) can be used to simultaneously fit electronic and protonic conductivity of the catalyst layer. However, it has not been applied in the literature to analyze experimental impedance spectra.

When oxygen transport is fast or the applied frequency is sufficiently high, $Z_{\rm ox}$ vanishes from equation (17) and the total impedance is given by equation (18). The latter, in contrast to equation (11), contains the HFR that can be found by taking the limit of $Z_{\rm ct+pe}$ at $\omega \to \infty$ [49]:

$$R_{\rm HF}^{\rm K} = \frac{L}{\sigma_{\rm H^+}^{\rm eff} + \sigma_{\rm e^-}^{\rm eff}}. \tag{19}$$

Note that the HFR depends on both protonic and electronic conductivity. The reason for this is best illustrated with the transmission-line representation of the catalyst layer. When ω is large, capacitors in the transmission line shown in Figure 2 act as shorts. If electronic resistance is negligible, current flows through the electronically conductive network (the bottom line) and the observed HFR is zero, as predicted by equation (15). In contrast, if the resistance of neither of the two conductive phases can be neglected, current flows through portions of each ohmic-resistance network. In this case, the observed HFR is non-zero and is composed of a portion of the electronic resistance and a portion of the protonic resistance of the CL, as seen in equation (19). If one of the conductivities is known, the other one can be estimated from the HFR using equation (19).

The low-frequency limit of equation (17) gives the DC resistance [49]:

$$R_{\rm DC}^{\rm K} = \frac{b}{i} + \frac{L}{3\sigma_{\rm H^+}^{\rm eff}} + \frac{L}{3\sigma_{\rm e^-}^{\rm eff}} + \frac{bL}{12FD_{\rm O_2}^{\rm eff}c^0}. \tag{20}$$

The four terms in the equation above describe the charge-transfer resistance, effective ohmic resistance due to proton and electron transport, and oxygen-transport resistance. Note that the ohmic-resistance terms

$$R_{\rm H^+}^{\rm K} = \frac{L}{3\sigma_{\rm H^+}^{\rm eff}}, \quad R_{\rm e^-}^{\rm K} = \frac{L}{3\sigma_{\rm e^-}^{\rm eff}} \tag{21}$$

were derived directly from the governing equations and differ from equation (14) by a factor of 3.

The applicability of equation (17) is limited to small current densities that satisfy [49]

$$i \ll \min\left\{ i_{\rm H^+}^* = \frac{\sigma_{\rm H^+}^{\rm eff} b}{L},\, i_{\rm e^-}^* = \frac{\sigma_{\rm e^-}^{\rm eff} b}{L},\, i_{\rm ox} \right\}. \tag{22}$$

The characteristic current density for electron transport, $i_{\rm e^-}^*$, was not included in condition (22) in the original work [49], but must naturally appear in it in the general case when electronic resistance cannot be neglected. For the parameters listed in Tables 2 and 3, condition (22) becomes $i \ll 0.1$ A/cm^2.

3.2. H_2/N_2 spectroscopy

3.2.1. Estimation of proton-transport properties

During the H_2/N_2 EIS measurements, no faradaic reaction occurs in the nitrogen-fed catalyst layer. In this case, impedance is obtained by assuming infinitely large charge-transfer resistance in equation (11) [19,48]:

$$Z^{\rm EKM} = \sqrt{\frac{R_{\rm H^+}^{\rm EKM}}{i\omega C_{\rm dl}^{*\,\rm EKM}}} \coth \sqrt{i\omega R_{\rm H^+}^{\rm EKM} C_{\rm dl}^{*\,\rm EKM}}. \tag{23}$$

This analytical model has been actively used in the literature to extract the catalyst-layer protonic-transport properties from the impedance spectra of PEMFCs[10,19–27,39], DMFCs[45], and PEMWEs[471].

At high frequencies, equation (23) is equivalent to equation (11), and thus equation (16) holds for H_2/N_2 EIS as well. As the frequency approaches infinity, impedance given by equation (23) approaches zero due to the assumption of high electronic conductivity of the catalyst layer. The Taylor-series expansion of equation (23) around zero frequency yields[19]

$$Z^{\mathrm{EKM}} = \frac{R_{\mathrm{H^+}}^{\mathrm{EKM}}}{3} + \frac{1}{i\omega C_{\mathrm{dl}}^{*\,\mathrm{EKM}}}. \tag{24}$$

As frequency tends to zero, impedance computed from equation (24) tends to the negative imaginary infinity. This results in a vertical line in the Nyquist plot located at $R_{\mathrm{H^+}}^{\mathrm{EKM}}/3$, which suggests that the protonic resistance of the CL is obtained by multiplying the length of the projection of the linear high-frequency impedance branch onto the real axis by 3 (this result can also be found in earlier works by Lefebvre et al.[63,96]). Equation (24) has been used to estimate protonic resistance and conductivity of fuel-cell[12,28–38,42] and electrolyzer[16,47] catalyst layers.

3.2.2. Simultaneous estimation of proton- and electron-transport properties

Because H_2/N_2 spectroscopy is a particular case of H_2/O_2 spectroscopy performed at zero oxygen concentration and at zero current, taking the limit of equation (17) at $i \to 0$ and $c^0 \to 0$ results in the following impedance for H_2/N_2 EIS[49]:

$$Z^{\mathrm{K}} = \frac{L}{\sigma_{\mathrm{H^+}}^{\mathrm{eff}}} \frac{\mathrm{i}q_0 \sin(p_0) + (1+\mathrm{i})\left(2k_\sigma + \left(1+k_\sigma^2\right)\cos(p_0)\right)}{k_\sigma\left(\mathrm{i}q_0 - (1+\mathrm{i})p_0\right)\sin(p_0)}, \tag{25}$$

where

$$p_0 = \sqrt{-\mathrm{i}\hat{\Omega}\left(1+\frac{1}{k_\sigma}\right)},$$

$$q_0 = \sqrt{-2k_\sigma\left(1+k_\sigma\right)\hat{\Omega}}.$$

This model has been recently used to estimate electronic and protonic conductivity of Fe-N-C catalyst layers for PEMFCs[97].

Impedance computed with equation (25) is equivalent to that found from equation (17) at high frequencies and results in the same HFR given in equation (19). Expansion of equation (25) around $\hat{\Omega} = 0$ ($\omega = 0$) was not given in reference[49], but it is provided here (taking only the leading terms proportional to $\hat{\Omega}^{-1}$ and $\hat{\Omega}^0$):

$$Z^{\mathrm{K}} = \frac{L}{3\sigma_{\mathrm{H^+}}^{\mathrm{eff}}} + \frac{L}{3\sigma_{\mathrm{e^-}}^{\mathrm{eff}}} + \frac{1}{\mathrm{i}\omega C_{\mathrm{dl}} L}, \tag{26}$$

where the first two terms are the DC resistance:

$$R_{\mathrm{DC}}^{\mathrm{K}} = \frac{L}{3\sigma_{\mathrm{H^+}}^{\mathrm{eff}}} + \frac{L}{3\sigma_{\mathrm{e^-}}^{\mathrm{eff}}}. \tag{27}$$

When the catalyst layer is highly electronically conductive, equation (26) is equivalent to equation (24) (with $C_{\mathrm{dl}}^{*\,\mathrm{EKM}} = C_{\mathrm{dl}} L$). However, there is an important difference between these two impedance relations; it is illustrated in Figure 3. When electronic conductivity is not significantly higher than protonic conductivity, impedance analysis with equations (23) and (24) will provide ohmic resistance equal to $R_{\mathrm{DC}} - R_{\mathrm{HF}}$ and will interpret it as a third of the

[1] A generalized form of equation (23) with constant-phase elements was used in references[24–26,39,45].

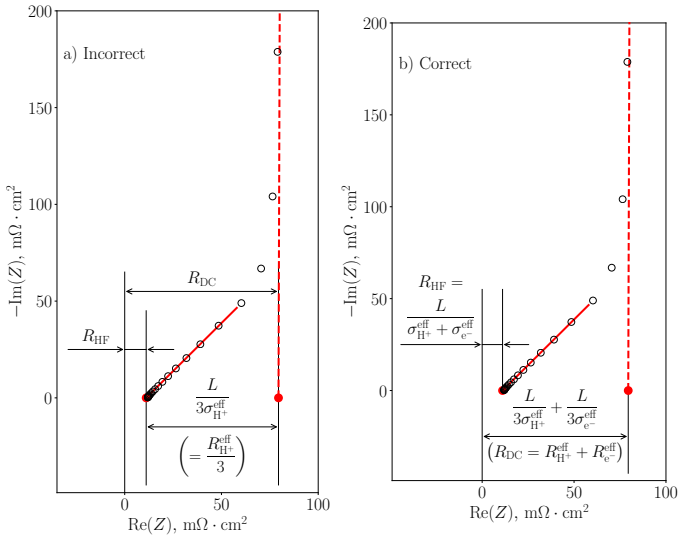

Figure 3: Illustration of the fitting procedure for an H_2/N_2 homogeneous-catalyst-layer spectrum using the graphical approach when $\sigma^{\mathrm{eff}}_{\mathrm{e^-}} \gg \sigma^{\mathrm{eff}}_{\mathrm{H^+}}$ does not hold: a) incorrect interpretation with equation (24); b) correct interpretation with equations (19) and (26). Hollow markers represent the numerical spectrum simulated for case IV (every fifth point is shown). Solid and dashed red lines represent the linear high-frequency and low-frequency fits, respectively. The low-frequency fit was obtained with the data at 1–1.6 Hz ($\mathrm{Im}(Z) > 4\ \Omega \cdot \mathrm{cm}^2$).

effective protonic resistance (Figure 3(a)). If equations (25) and (27) are used, both R_{HF} and R_{DC} will be correctly identified and the latter will be composed of the effective protonic and electronic resistances (Figure 3(b)).

Equations (19) and (26) provide a more accurate (compared to equation (24)) graphical approach to estimating the proton-transport properties of the catalyst layers that is shown in Figure 3(b). The protonic and electronic conductivities can be found by solving the system of algebraic equations (19) and (27). There are two pairs $(\sigma^{\mathrm{eff}}_{\mathrm{H^+}}, \sigma^{\mathrm{eff}}_{\mathrm{e^-}})$ that satisfy that system:

$$\sigma^{\mathrm{eff}}_{\mathrm{H^+}} = \frac{L}{2R^{\mathrm{K}}_{\mathrm{HF}}}\left(1 \pm \sqrt{1 - \frac{4R^{\mathrm{K}}_{\mathrm{HF}}}{3R^{\mathrm{K}}_{\mathrm{DC}}}}\right), \tag{28}$$

$$\sigma^{\mathrm{eff}}_{\mathrm{e^-}} = \frac{L}{2R^{\mathrm{K}}_{\mathrm{HF}}}\left(1 \mp \sqrt{1 - \frac{4R^{\mathrm{K}}_{\mathrm{HF}}}{3R^{\mathrm{K}}_{\mathrm{DC}}}}\right). \tag{29}$$

The fact that two pairs of distinct solutions to equations (19) and (27) exist means that two catalyst layers with the same but swapped protonic and electronic conductivities exhibit the same high-frequency spectrum. The numerical simulations performed in this work show that this is true, in fact, for the whole spectrum and holds in the frequency domain as well. This result is expected from equations (2) and (3), which are the same in $\phi_{\mathrm{H^+}}$ for the protonic current and $\phi_{\mathrm{e^-}}$ for the electronic current as long as E_{th} is constant and uniform in the layer (i.e., under the isobaric, isothermal condition). Note that the expression under the square root in equations (28) and (29) is non-negative (due to non-negative conductivities) and becomes zero when $\sigma^{\mathrm{eff}}_{\mathrm{H^+}} = \sigma^{\mathrm{eff}}_{\mathrm{e^-}}$.

3.3. Fitting approach

The impedance spectra computed through a direct numerical simulation of equations (1)–(3) were analyzed with the analytical relations given in equations (16), (18), (23), (24), (25), (28) and (29) in order to assess the ability of the latter to provide the correct charge-transport properties of the catalyst layers. Since only the ohmic properties

were of interest, the analytical-model fitting was limited to the linear high-frequency portion of each impedance spectrum. This portion was identified as a part of the high-frequency spectrum where the HFR-corrected real part and the imaginary part were within 2% from each other. In order to ensure the intermediate region between the linear branch and the charge-transport arc was not included in the fitting, the latter was limited to data points with the real part below a certain threshold. That threshold, found through visual inspection of the spectra, was 120 $\mathrm{m\Omega \cdot cm^2}$ in case IV and 60 $\mathrm{m\Omega \cdot cm^2}$ in other cases (except case III that was not fitted as discussed later). Only ohmic-resistance and conductivity values were treated as fitting parameters, and the rest of the parameters were taken form Table 2.

Equation (16) was fitted to both H_2/O_2 and H_2/N_2 spectra using the linear least-squares regression algorithm available in SciPy[88]. The sequential least-squares programming method from SciPy[88] was used to fit the H_2/N_2 spectra with equation (23). The residual of the fitting was defined as the root-mean-square deviation between the numerical and the analytical spectra:

$$\text{Residual} = \sqrt{\frac{\sum_{n=1}^{N} \left| Z_{\text{num}}(\omega_n) - Z_{\text{an}}(\omega_n) \right|^2}{N}}, \tag{30}$$

where N is the number of points in the portion of the spectrum to be fitted. Equations (18) and (25) were fitted to the H_2/O_2 and H_2/N_2 spectra, respectively, by minimizing the residual defined in equation (30). In this case, residuals were computed on a two-dimensional grid of 38–69 protonic and electronic conductivities spanning around the expected values. Then, the minimum point was found and refined by subsequently applying the Nelder-Mead (downhill simplex) minimization from SciPy[88]. The graphical approaches shown in Figure 3 were used to extract the protonic-transport properties from the H_2/N_2 spectra without any fitting as suggested by equations (24), (28), and (29). The position of the vertical low-frequency branch was determined from a linear fit of the 5 data points at the lowest frequencies of about 1–1.6 Hz.

Protonic-resistance estimates obtained with equations (16), (23), and (24) were converted into conductivity values using equation (14) in accordance with reference[48]. Protonic and electronic conductivities estimated with equations (18) and (25) were converted into resistances using equation (27) as discussed in reference[49] and in this work. The quality of the conductivity estimates was assessed by comparing the fitted values to the exact effective conductivities listed in Table 3. The fitted ohmic resistances were compared to the numerical predictions obtained through ohmic heating as shown in equations (6) and (7).

The developed Python script for estimating catalyst-layer charge-transport properties with equations (18) and (25) and with the graphical method from Figure 3(b) has been made available at `https://github.com/OpenFCST/EIS/archive/main.zip`. Because catalyst-layer impedance is frequency-dependent, it is required that experimental data contain frequency of each impedance point.

4. Results and discussion

4.1. Model validation

The catalyst-layer model was first validated using the experimental impedance data measured by Makharia et al.[19] Two catalyst layers were considered, one with an ionomer-to-carbon weight ratio of 0.8 and another with a

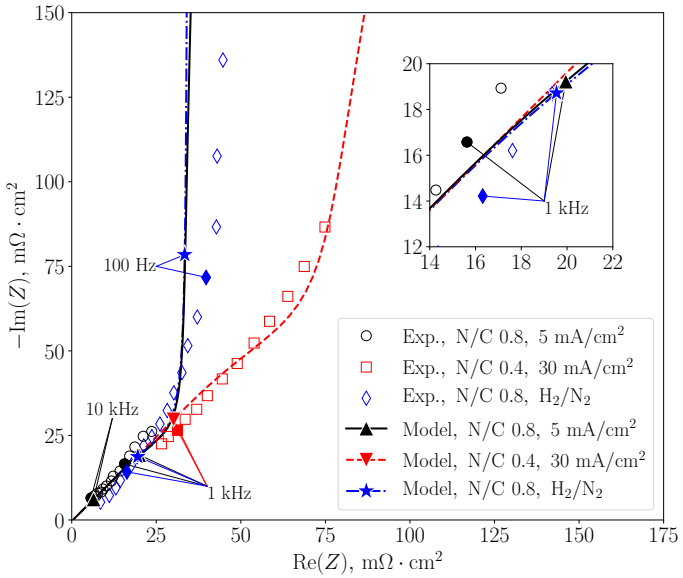

Figure 4: Comparison of the H_2/O_2 and H_2/N_2 spectra simulated numerically (lines) to those measured by Makharia et al.[19] Solid circles, squares, and diamonds represent experimental points for which frequency was reported. The corresponding simulated points are marked with triangles and stars.

ratio of 0.4, both 13-μm-thick[19]. The respective effective protonic conductivities were obtained from the reported protonic resistance values using equation (14) (assumed by Makharia et al. in their resistance estimation) and were approximately 13.0 mS/cm and 5.53 mS/cm. The volumetric double-layer capacitance was 16.2 F/cm^3[19]. The operating conditions were 80 °C, 270 kPa, and 100% RH[19]. The rest of the model parameters were unchanged. All experimental spectra were corrected by Makharia et al.[19] for the external inductance and the HFR. Since the catalyst layers were carbon-based, their electronic conductivity was relatively high, and the correction performed with the whole measured HFR did not significantly affect the catalyst-layer impedance.

The simulated and the experimental spectra are compared in Figure 4. Only high-frequency data from reference[19] were considered, as impedance at low frequencies may have been affected by physical phenomena taking place in the cell components that are not accounted for in the model (for example, mass transport in gas-diffusion layers). A reasonable agreement was achieved under both H_2/O_2 and H_2/N_2 conditions. Frequency of only a handful of data points was reported in reference[19]; those points are shown in Figure 4 as filled markers (circles, squares, and diamonds) and are labeled. The points in the simulated spectra that correspond to the reported frequencies are marked with triangles and stars and are labeled. The simulated impedance points at 0.1, 1, and 10 kHz were in close proximity of their experimental counterparts. The discrepancy between the simulated and the experimental H_2/N_2 spectra at frequencies around and below 100 Hz may be due to hydrogen cross-over in the tested cell[20,21]. As expected, the simulated H_2/N_2 spectrum coincided with the H_2/O_2 spectrum at 5 mA/cm^2 in the shown frequency range.

An additional validation was performed by comparing the impedance spectra simulated for homogeneous catalyst layers to the spectra predicted by equations (17) and (25) with varied conductivities from Table 3. The H_2/O_2 spectra computed at 0.01 and 0.1 A/cm^2 are shown in Figures 5 and 6. In this work, most spectra are reported in four plots for completeness and clarity. The Nyquist plots are provided in Figures 5(a) and 6(a); they show the characteristic

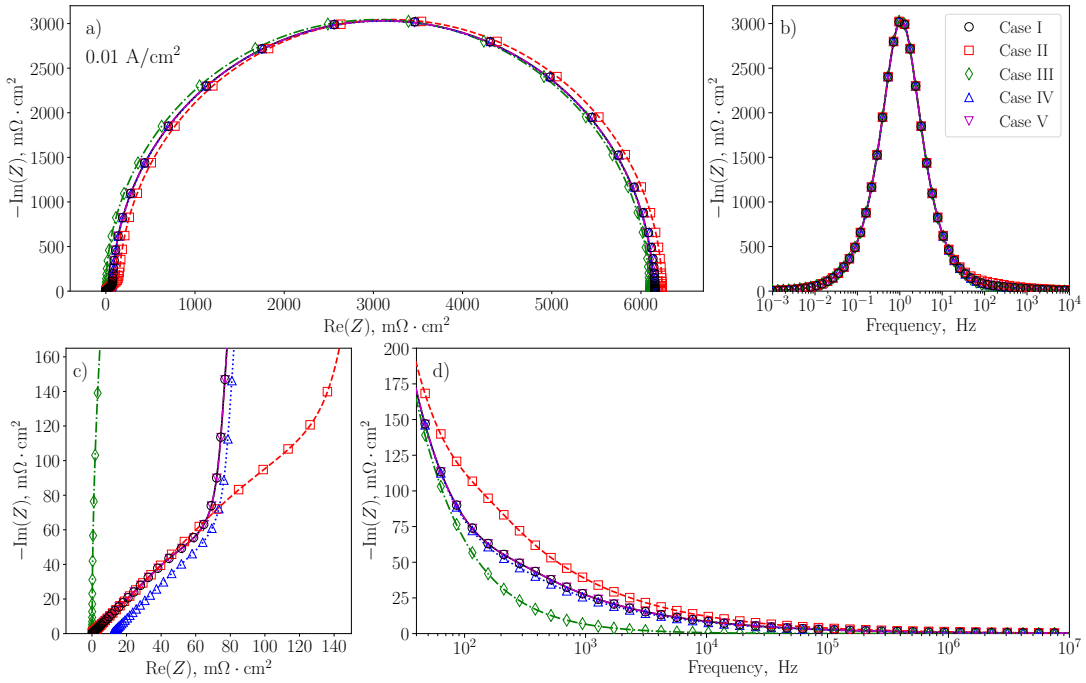

Figure 5: Comparison of the H_2/O_2 spectra simulated numerically (markers) to those computed analytically with equation (17) (lines) at 0.01 A/cm^2: a), c) Nyquist plot and its high-frequency portion; b), d) Bode plot of the imaginary impedance component and its high-frequency portion. Every twentieth point is shown for clarity.

resistances, such as R_{HF} and R_{DC}. The Bode plots in Figures 5(b) and 6(b) display the frequency composition of the spectra, including the frequency of their main capacitive arcs. The inclusion of the Bode plot is required to eliminate the ambiguity of the Nyquist plot: multiple cell-parameter sets can lead to the same Nyquist plot, but the frequency range in the Bode plot will differ[98]. The enlarged Nyquist plots in Figures 5(c) and 6(c) allow for a clear visualization of the high-frequency linear branches of the spectra and their R_{HF}. The frequency composition of those branches is given in the enlarged Bode plots (Figures 5(d) and 6(d)).

The agreement with the analytical model (17) was good at 0.01 A/cm^2 with some minor deviations at frequencies below 10 Hz at 0.1 A/cm^2, in alignment with the limiting condition (22). The discrepancy between the numerical and the analytical predictions increased as the current density exceeded the validity range of equation (17), as demonstrated in Figures S1 and S2 of the Supplementary Information.

The agreement between the numerically simulated H_2/N_2 spectra and those computed with equation (25) was good (Figure 7). As expected, the high-frequency H_2/N_2 spectra in Figure 7(b) resembled those in the H_2/O_2 spectra at 0.01 A/cm^2 in Figure 5(c).

In all of the considered cases, the numerical model was also able to correctly predict the shape of the high-frequency portion of the spectrum. In accordance with equation (21) and Figure 3(b), the length of the linear 45° branch increased as the protonic conductivity decreased between cases I and II. When both conductivities were high (case III), the real-axis projection of the linear branch became negligible at less than 0.04 mΩ·cm^2. The HFR of the catalyst layer with poor electron conductivity (case IV) was about 11.9 mΩ·cm^2 and was significant compared to the overall length of the linear branch. This value was reasonably close to the theoretical result of 11.3 mΩ·cm^2 found from equation (19). Due to the sensitivity of the HFR to the numerical error, it is not reported for other parametric

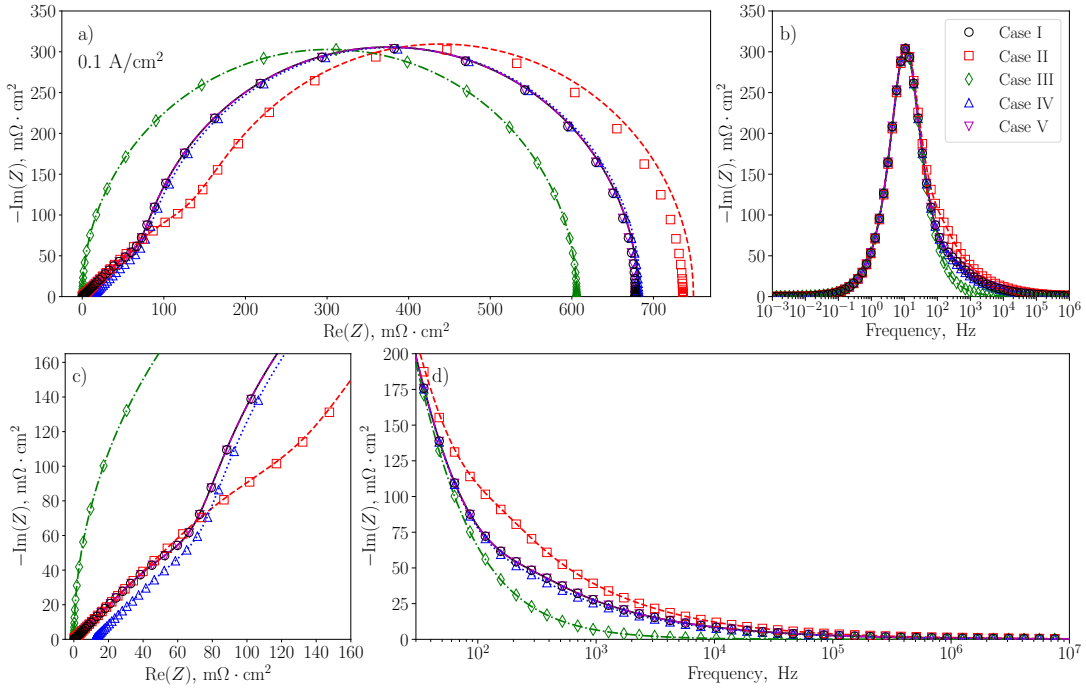

Figure 6: Comparison of the H_2/O_2 spectra simulated numerically (markers) to those computed analytically with equation (17) (lines) at 0.1 A/cm^2: a), c) Nyquist plot and its high-frequency portion; b), d) Bode plot of the imaginary impedance component and its high-frequency portion. Every twentieth point is shown for clarity.

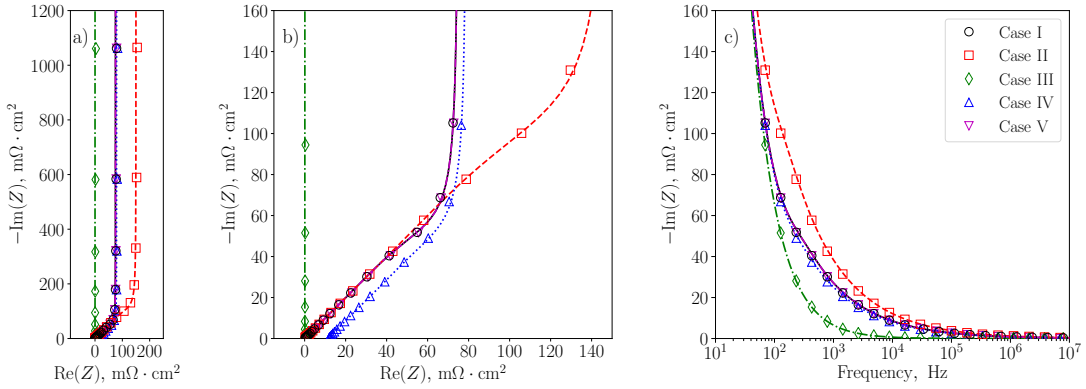

Figure 7: Comparison of the H_2/N_2 spectra simulated numerically (markers) to those computed analytically with equation (25) (lines): a), b) Nyquist plot and its high-frequency portion; c) Bode plot of the imaginary impedance component (high-frequency portion). Every fifth point is shown for clarity.

cases, where this resistance was about 0.1 $\mathrm{m\Omega \cdot cm^2}$ or less. The impedance spectra for cases I and V were identical as these cases reflected two catalyst layers with swapped protonic and electronic conductivities. This was expected from the discussion of equations (28) and (29).

4.2. Effect of multi-step kinetics

Depending on the catalyst-layer properties and on the operating conditions, faradaic processes may take place at frequencies similar to those at which the linear 45° branch is observed, making it difficult to separate faradaic and charge-transport phenomena[56]. The frequency and the current density at which the linear impedance branch becomes independent of the faradaic processes (and thus of the reaction mechanism) was estimated analytically and numerically for PEMFCs operating under H_2/O_2 conditions.

The analytical estimation given next was inspired by the discussion in reference[56]. The characteristic angular frequency of a charge-transport process can be approximated as a reciprocal of the characteristic time constant $\tau = RC$[99,100] of a parallel RC circuit consisting of a double-layer capacitor and an ohmic resistor with resistance equal to the sum of the protonic and electronic resistances in equation (21):

$$\omega_\Omega = \frac{3\sigma_{\mathrm{H^+}}^{\mathrm{eff}}\sigma_{\mathrm{e^-}}^{\mathrm{eff}}}{\left(\sigma_{\mathrm{H^+}}^{\mathrm{eff}} + \sigma_{\mathrm{e^-}}^{\mathrm{eff}}\right) C_{\mathrm{dl}} L^2}. \tag{31}$$

Similarly, the characteristic frequency of a faradaic process can be estimated using charge-transfer resistance. As shown in Appendix A, the latter is given by $R_{\mathrm{ct}} = b/\left(i_0 A_{\mathrm{v}} L\right)$ when $\eta \approx 0$ and by $R_{\mathrm{ct}} = b/i$ in the Tafel regime (the latter appears in equation (20)). The two respective estimates are

$$\omega_{\mathrm{ct}} = \frac{i_0 A_{\mathrm{v}}}{b C_{\mathrm{dl}}}$$

and

$$\omega_{\mathrm{ct}} = \frac{i}{b C_{\mathrm{dl}} L}.$$

For the 45° branch to be free of the faradaic effects, ω_Ω must be sufficiently larger than ω_{ct} and impedance must be measured at a frequencies that satisfy the following:

$$\omega > \omega_\Omega \gg \omega_{\mathrm{ct}}. \tag{32}$$

This results in an upper limit of the recommended operating current density:

$$i \ll i_{\mathrm{HF}} = \omega_\Omega b C_{\mathrm{dl}} L. \tag{33}$$

For the catalyst-layer parameters given in Table 2 and electrical and protonic conductivities of 3.79 S/cm and 2 mS/cm, respectively (case I from Table 3), $f_\Omega = \omega_\Omega/(2\pi)$ is 87.3 Hz and i_{HF} is 0.811 $\mathrm{A/cm^2}$. Similar or less strict estimates were obtained for other cases considered in this work except for case III, where protonic conductivity was significantly higher than that in Nafion®-based CLs; in that case, f_Ω was 57.2 kHz and i_{HF} was 531 $\mathrm{A/cm^2}$. Therefore, in general, charge-transport characterization of Nafion®-based PEFMC and PEMWE catalyst layers via EIS should be performed either under H_2/O_2 conditions at or below 10 $\mathrm{mA/cm^2}$ or under H_2/N_2 conditions; the applied frequency range should exceed 1 kHz. The same limitations apply to the analytical models discussed in Section 3 due to the assumed Tafel kinetics.

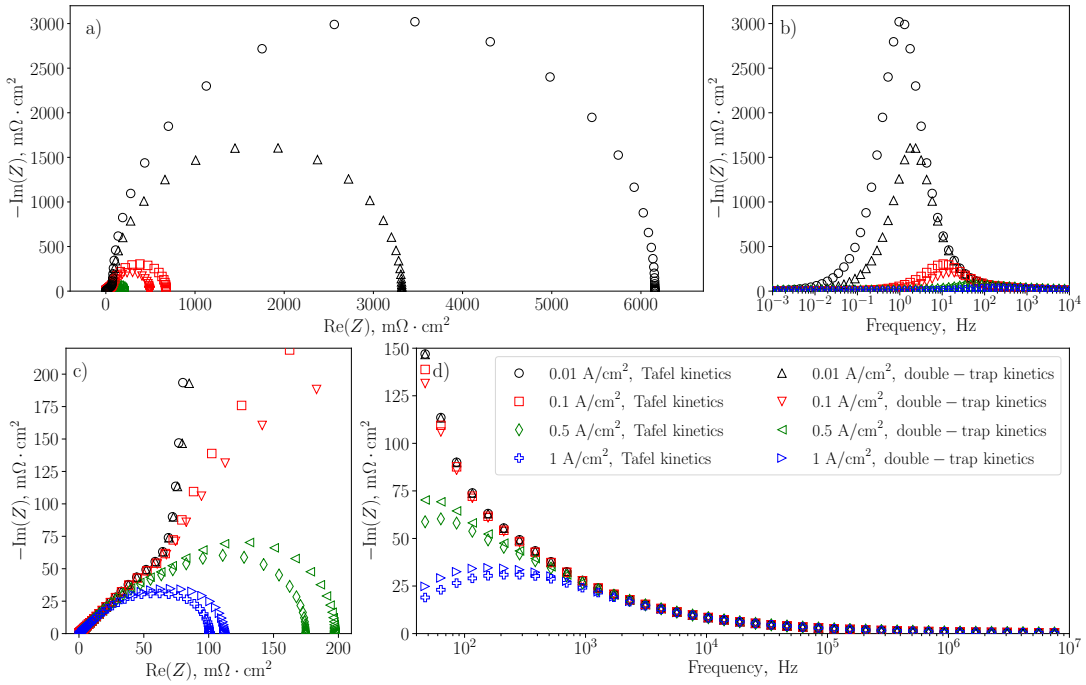

Figure 8: Comparison of the H_2/O_2 spectra simulated numerically for case I using the Tafel and the double-trap ORR kinetics: a), c) Nyquist plots; b), d) Bode plots of the imaginary impedance component. Every twentieth point is shown for clarity.

Spectra simulated for case I from Table 3 using Tafel kinetics (equation (4)) and double-trap kinetics (equation (5)) were compared (Figure 8). The frequency at which impedance became independent of the faradaic effects was estimated as the frequency at which the spectra computed with the two kinetic models started to deviate by more than 2% at high frequencies[2]. The threshold frequency increased with current density and was 61.8, 129, 550, and 1,216 Hz at 0.01, 0.1, 0.5, and 1 A/cm^2, respectively. This was in agreement with equations (31)–(33) that limited the catalyst-layer charge-transport characterization to $f > 87.3$ Hz and $i \ll 0.811$ A/cm^2 for the given CL parameters.

4.3. Assessment of the analytical models for homogeneous catalyst layers

4.3.1. H_2/O_2 spectroscopy

The numerical H_2/O_2 spectra simulated at 0.01, 0.1, 0.5, and 1 A/cm^2 (Figures 5, 6, S1, and S2) were analyzed with equations (16) and (18) using the methodology discussed earlier (equation (17) was reduced to equation (18) due to no oxygen-transport limitations). In case of equation (18), conductivities were fitted and then converted into resistances using equation (21). The fitted protonic and electronic resistances are given in Table 4 along with those resistances computed in the numerical model via ohmic heating (equations (6) and (7)). The R^2 of the fitting was at least 0.999. No resistance is reported in case III as it was not possible to achieve a reliable fit due to the significant effect of the numerical error on the small high-frequency branch (less than 0.04 $\mathrm{m\Omega \cdot cm^2}$ in the real component). Plots of the fitted spectra can be found in Figures S3 and S4 of the Supplementary Information.

[2]The differences between the spectra simulated at the same current density were solely due to the faradaic process since the oxygen-transport effects were negligible. The latter was confirmed by performing additional simulations with a 10 times higher oxygen diffusivity and observing no change in the spectra.

Table 4: Catalyst-layer protonic and electronic resistances fitted to the H_2/O_2 spectra using equations (16) and (18) along with those resistances estimated via ohmic heating with equations (6) and (7). In case of equation (18), conductivities were fitted and then converted into resistances using equation (21). Two resistance pairs given in case V for equation (18) resulted in similar, within 10^{-11} $m\Omega \cdot cm^2$, residuals (resistance corresponding to the smaller residual is given first).

Case	$\boldsymbol{R^{EKM}_{H^+}}$, $\mathbf{m\Omega \cdot cm^2}$ **(Fit, Eq.** (16)**)**	$\boldsymbol{R^{K}_{H^+}}$, $\mathbf{m\Omega \cdot cm^2}$ **(Fit, Eq.** (18)**)**	$\boldsymbol{R^{K}_{e^-}}$, $\mathbf{m\Omega \cdot cm^2}$ **(Fit, Eq.** (18)**)**	$\boldsymbol{R^{eff}_{H^+}}$, $\mathbf{m\Omega \cdot cm^2}$ **(Est., Eq.** (6)**)**	$\boldsymbol{R^{eff}_{e^-}}$, $\mathbf{m\Omega \cdot cm^2}$ **(Est.,Eq.** (7)**)**
			0.01 A/cm^2		
I	226	75.0	0.0396	**74.6**	**0.0398**
II	452	150	0.0422	**149**	**0.0399**
IV	182	75.0	3.95	**74.6**	**3.98**
V	231	75.3, 0.141	0.141, 75.3	**0.0398**	**74.6**
			0.1 A/cm^2		
I	225	74.9	0.0453	**71.4**	**0.0413**
II	449	150	0.0494	**136**	**0.0430**
IV	187	74.9	3.98	**71.6**	**4.12**
V	228	0.151, 75.2	75.2, 0.151	**0.0413**	**71.4**
			0.5 A/cm^2		
I	224	74.7	0.0544	**59.4**	**0.0476**
II	448	149	0.0562	**97.2**	**0.0542**
IV	192	74.1	4.06	**60.2**	**4.70**
V	222	0.200, 74.4	74.4, 0.200	**0.0476**	**59.4**
			1 A/cm^2		
I	224	74.3	0.0607	**48.6**	**0.0542**
II	447	149	0.0590	**70.6**	**0.0640**
IV	189	73.1	4.10	**49.9**	**5.30**
V	220	0.230, 73.3	73.3, 0.230	**0.0543**	**48.5**

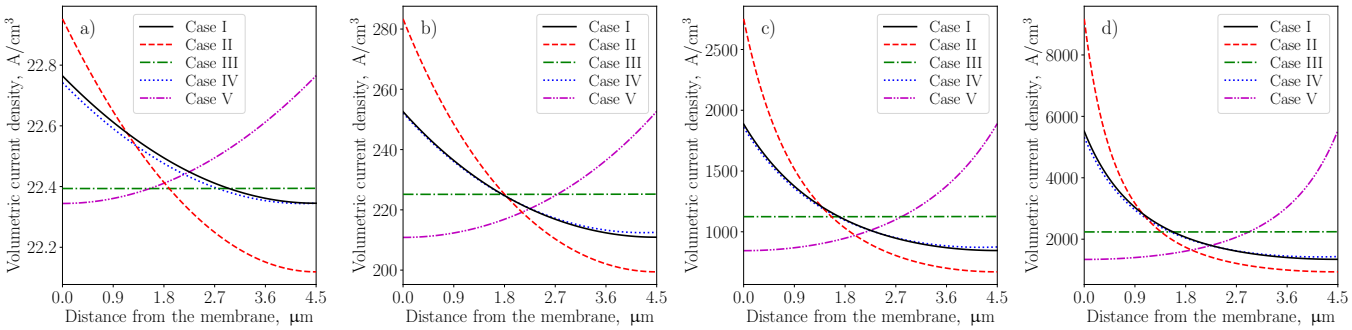

Figure 9: Comparison of the simulated steady-state volumetric-current-density distributions in the catalyst layer at: a) 0.01 A/cm^2; b) 0.1 A/cm^2; c) 0.5 A/cm^2; and d) 1 A/cm^2. The membrane is located at the left end and the microporous/gas-diffusion layer is located at the right end of each graph.

Table 4 shows that the protonic resistance fitted with equation (18) closely matched the numerical estimate (which has the meaning of the resistance necessary to dissipate the heat produced in the protonically conductive phase due to ohmic heating) at 0.01 A/cm^2 in cases I, II, and IV. On the other hand, equation (16) resulted in a threefold overestimation of it. Therefore, the correct interpretation of equations (16) and (24) is that the effective protonic resistance of a catalyst layer (that has high electronic conductivity) is a third of $R_{H^+}^{EKM}$ (defined by equation (14)), which is in agreement with the results obtained by Kulikovsky[49] (equation (21)). Equation (16) performed the worst in case IV due to the assumed high electronic conductivity of the CL. The electronic resistance fitted with equation (18) was reasonably accurate at 0.01 A/cm^2 in cases II and IV. The reason for the relatively poor electronic-resistance fits will be discussed shortly.

The two resistance values obtained in case V correspond to the two search regions used in the fitting: the first region corresponded to the exact conductivities used in the simulations and the second region covered the swapped conductivities (i.e., those from case I). The fitting residuals at the two optimum points were nearly the same (within 10^{-11} m$\Omega \cdot$ cm^2), as expected from the discussion of equations (28) and (29). This means that the assignment of the fitted charge-transport properties to one of the two conductive phases of a CL is not possible without knowing which of the phases is more conductive.

Deviation between the analytical fits and the numerical resistance increased with current density. The numerical model showed a gradual decrease in the protonic resistance and a gradual increase in the electronic resistance (in cases I, II, and IV; vice versa in case V) as more and more current was produced at the catalyst-layer/membrane interface (or at the CL-PTL interface in case V; Figure 9), affecting the travel distance of protons and electrons. This was not captured with the analytical equations (16) and (18).

The conductivity values corresponding to the resistances from Table 4 are listed in Table 5. In case of equation (16), the fitted resistance was converted into conductivity using equation (14). Both analytical models (16) and (18) produced reasonably good conductivity estimates for the less conductive phase at all current densities. Therefore, equation (16) can be used to extract the lower of the two conductivities from the impedance spectrum, despite the resistance overestimation, as long as equation (14) is used for the conversion. It is worth noting that conductivity estimated using EIS is reported less often in the literature than resistance (some examples are references[10,20,23,34,36,37,39,40,42,44]).

Table 5: Catalyst-layer protonic and electronic conductivities fitted to the H_2/O_2 spectra using equations (16) and (18) along with the exact conductivities from Table 3. In case of equation (16), resistance was fitted and then converted into conductivity using equation (14). Two conductivity pairs given in case V for equation (18) resulted in similar, within 10^{-11} $m\Omega \cdot cm^2$, residuals (conductivity corresponding to the smaller residual is given first).

Case	$\boldsymbol{\sigma^{EKM}_{H^+}}$**, mS/cm (Fit, Eq.** (16)**)**	$\boldsymbol{\sigma^{K}_{H^+}}$**, mS/cm (Fit, Eq.** (18)**)**	$\boldsymbol{\sigma^{K}_{e^-}}$**, mS/cm (Fit, Eq.** (18)**)**	$\boldsymbol{\sigma^{eff}_{H^+}}$**, mS/cm (Model input, Table 3)**	$\boldsymbol{\sigma^{eff}_{e^-}}$**, mS/cm Model input, (Table 3)**
			0.01 A/cm^2		
I	1.99	2.00	3788	**2.00**	**3788**
II	0.996	1.00	3553	**1.00**	**3788**
IV	2.47	2.00	38.0	**2.00**	**37.9**
V	1.95	1.99, 1065	1065, 1.99	**3788**	**2.00**
			0.1 A/cm^2		
I	2.00	2.00	3311	**2.00**	**3788**
II	1.00	1.00	3037	**1.00**	**3788**
IV	2.41	2.00	37.7	**2.00**	**37.9**
V	1.98	992, 1.99	1.99, 992	**3788**	**2.00**
			0.5 A/cm^2		
I	2.01	2.01	2759	**2.00**	**3788**
II	1.00	1.00	2667	**1.00**	**3788**
IV	2.34	2.02	37.0	**2.00**	**37.9**
V	2.02	751, 2.02	2.02, 751	**3788**	**2.00**
			1 A/cm^2		
I	2.01	2.02	2470	**2.00**	**3788**
II	1.01	1.01	2540	**1.00**	**3788**
IV	2.38	2.05	36.6	**2.00**	**37.9**
V	2.04	653, 2.05	2.05, 653	**3788**	**2.00**

Table 6: Catalyst-layer protonic and electronic resistances fitted to the H_2/N_2 spectra using the two graphical approaches illustrated in Figure 3 and equations (16), (23), and (25), along with the reference resistances computed with equation (21). In case of equation (25), conductivities were fitted and then converted into resistances using equation (21). The modified graphical approach from Figure 3(b) resulted in two equally valid pairs of protonic and electronic resistances. Two resistance pairs given in case V for equation (25) resulted in similar, within 10^{-11} $m\Omega \cdot cm^2$, residuals (resistance corresponding to the smaller residual is given first).

Case	$R^{EKM}_{H^+}$, $m\Omega \cdot cm^2$ **(Fit, Fig. 3(a))**	$R^{K}_{H^+}$, $m\Omega \cdot cm^2$ **(Fit, Fig. 3(b))**	$R^{K}_{e^-}$, $m\Omega \cdot cm^2$ **(Fit, Fig. 3(b))**	$R^{EKM}_{H^+}$, $m\Omega \cdot cm^2$ **(Fit, Eq.** (16)**)**	$R^{EKM}_{H^+}$, $m\Omega \cdot cm^2$ **(Fit, Eq.** (23)**)**	$R^{K}_{H^+}$, $m\Omega \cdot cm^2$ **(Fit, Eq.** (25)**)**	$R^{K}_{e^-}$, $m\Omega \cdot cm^2$ **(Fit, Eq.** (25)**)**	$R^{K}_{H^+}$, $m\Omega \cdot cm^2$ **(Est, Eq.** (21)**)**	$R^{K}_{e^-}$, $m\Omega \cdot cm^2$ **(Est, Eq.** (21)**)**
I	226	75.5, 0.0271	0.0271, 75.5	218	216	72.4	0.0722	**75**	**0.0396**
II	453	151, 0.0224	0.0224, 151	437	434	145	0.0848	**150**	**0.0396**
IV	227	75.6, 3.89	3.89, 75.6	162	180	71.8	3.96	**75**	**3.96**
V	231	75.3, 0.490	0.490, 75.3	207	212	72.5, 0.319	0.319, 72.5	**0.0396**	**75**

The quality of the fits obtained with equation (18) for the more conductive phase was relatively poor in Tables 4 and 5. This was due to the lower sensitivity of the catalyst-layer impedance (e.g., equation (18)) to the dominating conductivity (see the discussion of Figure S5 in the Supplementary Information).

4.3.2. H_2/N_2 spectroscopy

The catalyst-layer charge-transport properties were extracted from the simulated H_2/N_2 spectra shown in Figure 7 using the two graphical approaches illustrated in Figure 3 and by fitting equations (16), (23), and (25). The R^2 of the fits was at least 0.999. Plots of the fitted spectra are provided in Figures S6 and S7 in the Supplementary Information.

In this case, the ohmic-heating-based approach to estimating the ohmic resistance of the catalyst layer (equations (6) and (7)) could not be used due to the current density being zero[3]. Instead, equation (21) was used to obtain the reference protonic and electronic resistances since its accuracy increases as current approaches zero.

The ohmic resistances extracted from the H_2/N_2 spectra are shown in Table 6. Similarly to the H_2/O_2-spectra fits, the resistances of the less conductive phase obtained from equations (16) and (23), as well as from the graphical method from Figure 3(a) (equation (24)), were about 3 times larger than the reference values with the worst fit in case IV. Interestingly, the modified graphical approach from Figure 3(b) resulted in more accurate resistances than those fitted with equation (25). This validates the graphical method in Figure 3(b), based on equations (28) and (29), as a novel and more convenient graphical method for estimating the catalyst-layer charge-transport properties.

The effective conductivities were extracted as before. Because substitution of equation (14) into equation (24) results in the same real impedance component at low frequencies as in equation (21), all of the considered methods provided good conductivity estimates for the less conductive phase (Table S1 of the Supplementary Information).

[3]Since the H_2/N_2 spectra were approximated in this work by the H_2/O_2 spectra computed with the oxygen-molar fraction of 10^{-10}, the produced current density was, in fact, 10^{-12} A/cm^2 by the order of magnitude. However, the potential gradients were also small, and, due to the limited-precision arithmetic, this resulted in the numerically inaccurate ohmic-heating-based resistances. Nevertheless, the computed impedance spectra were accurate, as evident from the presented results.

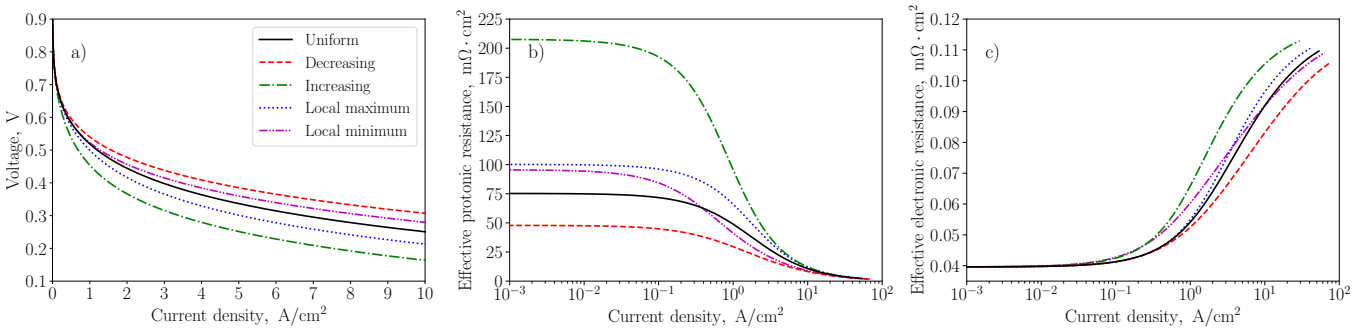

Figure 10: Comparison of the polarization curves (a) and ohmic resistances (b, c) of the catalyst layer simulated numerically for the ionomer-loading distributions from Figure 1. The ohmic resistance was computed through ohmic heating (equations (6) and (7)).

The resistance and conductivity estimates obtained with equation (25) and the corresponding graphical method were not as accurate for the more conductive phase. As a particular case of equation (18), equation (25) also has a lower sensitivity to the dominating conductivity. The residual graphs are provided in Figure S8 in the Supplementary Information.

4.4. Effect of heterogeneous ionomer loading

4.4.1. Polarization and ohmic-resistance curves

Before the impedance spectra of heterogeneous catalyst layers were analyzed, some insight on the resistance-conductivity relationship was gathered by performing DC polarization-curve simulations. The voltage-current relationships of the catalyst layers described in Figure 1 are shown in Figure 10(a). The catalyst-layer performance simulated in this work was relatively low and close to the performance of a whole cell (cf. references[62,69,70]) due to the chosen kinetic parameters. This, however, had no effect on the generality of the results and conclusions of this work that was focused on charge transport. The performance of a graded catalyst layer was higher when the zone located closer to the membrane was more conductive than all or most of the other zones (the "Decreasing" and the "Local minimum" cases). Gerteisen[76] reported a similar effect of the conductivity distribution in a CL.

Additional information can be obtained from the ohmic-heating analysis. The computed effective ohmic resistances are plotted in Figures 10(b) and 10(c). In all cases, similar protonic resistances were observed at current densities above 10 A/cm^2, while the electronic resistances converged as current densities decreased below 0.1 A/cm^2. This was due to the changing current-density distribution within the catalyst layer (Figures 11(a)–(d)) that affected the travel distances of protons and electrons.

Interestingly, the protonic resistance converged to different values in each case as current density tended to zero (Figure 10(b)). Those limiting values are provided in Table 7 and are accompanied with the analytical estimates obtained from equation (21) with the following three methods: a) averaging the protonic conductivity in the catalyst layer and then applying equation (21); b) averaging the resistances calculated for each zone; and c) summing the resistances of all zones due to the series connection. The ohmic-heating-based resistance was in agreement with the analytical estimate found from equation (21) only in the case of the uniform ionomer distribution. When the protonic conductivity varied in the catalyst layer, the effective protonic resistance significantly differed from the analytical estimates. This means that equation (21) cannot be used for heterogeneous CLs.

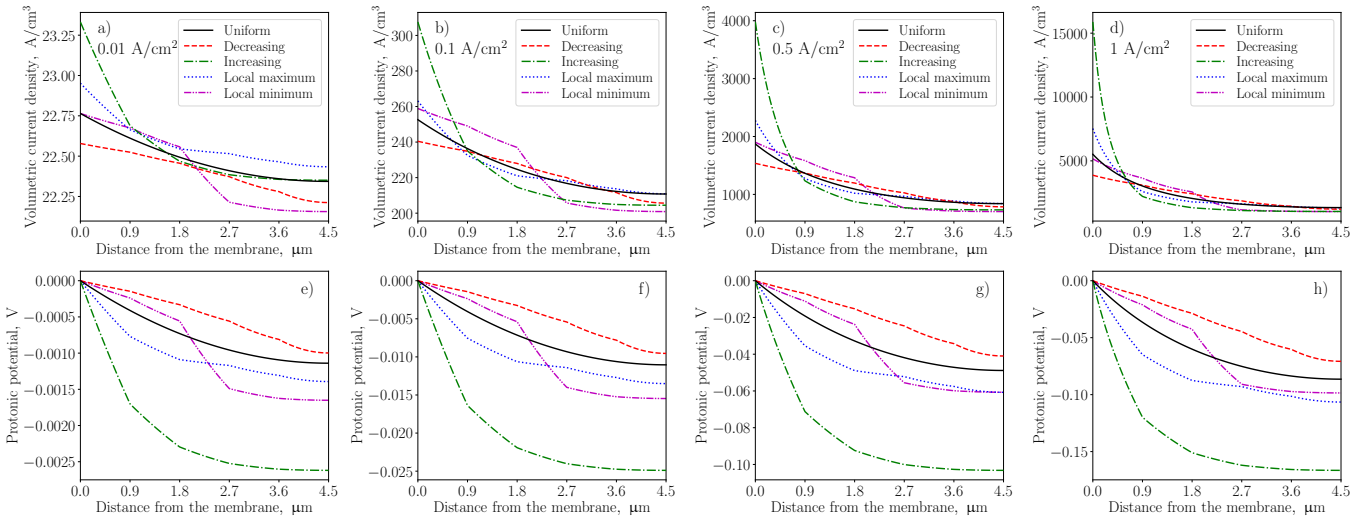

Figure 11: Comparison of the volumetric-current-density and protonic-potential distributions simulated for the ionomer-loading distributions from Figure 1 at: a), e) 0.01 A/cm^2; b), f) 0.1 A/cm^2; c), g) 0.5 A/cm^2; and d), h) 1 A/cm^2.

Table 7: Comparison of the ohmic-heating based protonic resistance computed at 0.1 mA/cm^2 using equation (6) to the analytical estimates obtained from equation (21) via the three methods explained in the text.

Distribution	$\boldsymbol{R^{\mathrm{eff}}_{\mathrm{H+}}}$, $\mathbf{m\Omega \cdot cm^2}$ **(Eq.** (6)**)**	$\boldsymbol{R^{\mathrm{K}}_{\mathrm{H+}}}$, $\mathbf{m\Omega \cdot cm^2}$ **(Eq.** (21)**)**		
		Method a)	**Method b)**	**Method c)**
Uniform	75.3	75.0	75.0	75.0
Decreasing	47.9	59.7	120	598
Increasing	208	59.7	120	598
Local maximum	100	64.0	91.6	458
Local minimum	95.7	66.4	110	550

To explain why the resistance-conductivity relationship (21) does not hold, the protonic-potential distributions were analyzed (Figures 11(e)–(h)). If the catalyst layer had only one conductive phase, its potential distribution would have been linear. Because it has two conductive phases, each of which terminates at one of the boundaries, the potential distribution is nonlinear even in the homogeneous case. It turns out that the shape of this distribution is such that equation (6) gives $L/\left(3\sigma_{\mathrm{H^+}}^{\mathrm{eff}}\right)$ only for homogeneous catalyst layers and at low current. As current density increased, the potential distribution started to change (Figure S9 in the Supplementary Information). Since equations (6) and (7) do not capture this effect, their estimates deviated from the ohmic-heating-based resistance (see Table 4).

4.4.2. H_2/O_2 spectroscopy

The H_2/O_2 EIS simulations were repeated with the model parameters from Figure 1. Uniform ionomer loading in the graded catalyst layer was used as a control case to ensure the results obtained with a single homogeneous catalyst layer were reproduced. The computed spectra are shown in Figures 12, 13, and in Figures S10, S11 in the Supplementary Information. In those figures, graphs of the phase angle (computed from the point $(R_{\mathrm{HF}}, 0)$) against frequency are provided to visualize the convergence of the slope of the high-frequency linear impedance branch to 45° (for example, Figure 12(d)). The shape of the spectrum varied significantly depending on the ionomer distribution. The decrease in the oxygen diffusivity due to the reduced porosity did not have an effect on the simulated spectra. This was confirmed by observing no change in the impedance spectrum computed in the increasing-ionomer-loading case at 1 A/cm^2 with a 10 times higher oxygen diffusivity.

As seen in Figures 12(d) and 13(c), the phase angle converged to -45° at about 10 kHz in all spectra and remained approximately constant until the frequency reached 100 kHz. At higher frequencies, the phase angle was very sensitive to the numerical error due to the small impedance magnitude. The spectra corresponding to the "decreasing" and the "local minimum" cases converged to -45° from a higher impedance slope (except for the latter case at 1 A/cm^2). In the "increasing" and "local maximum" cases, the intermediate region between the linear high-frequency branch and the charge-transfer arc transformed into a distinct capacitive arc at about 0.01-1 kHz (Figures 12(c) and 13(a)). The observed shape of the high-frequency spectra was in agreement with other modeling studies [21,55,76,77].

The ohmic-heating analysis performed in this work provides additional insight on whether the apparent linear impedance branch represents the total ohmic resistance of a heterogeneous catalyst layer. The total ohmic resistance computed with equations (6) and (7) is marked with vertical lines in Figures 12(c) and and 13(a), and the frequency at which it intersects with each spectrum is labeled. The real-axis projection of the apparent linear branch of the high-frequency spectrum was always shorter than the total ohmic resistance. Moreover, the junction point that indicates the total ohmic resistance may be located on a capacitive arc, as observed in the "increasing" and the "local-maximum" ionomer-distribution cases in Figure 13(a). At 1 A/cm^2, all catalyst layers exhibit seemingly similar high-frequency impedance, while their ohmic resistances vary significantly (Figure 10(b)). Therefore, no conclusions on the catalyst-layer charge-transport properties should be made from the qualitative comparison of the high-frequency spectra alone.

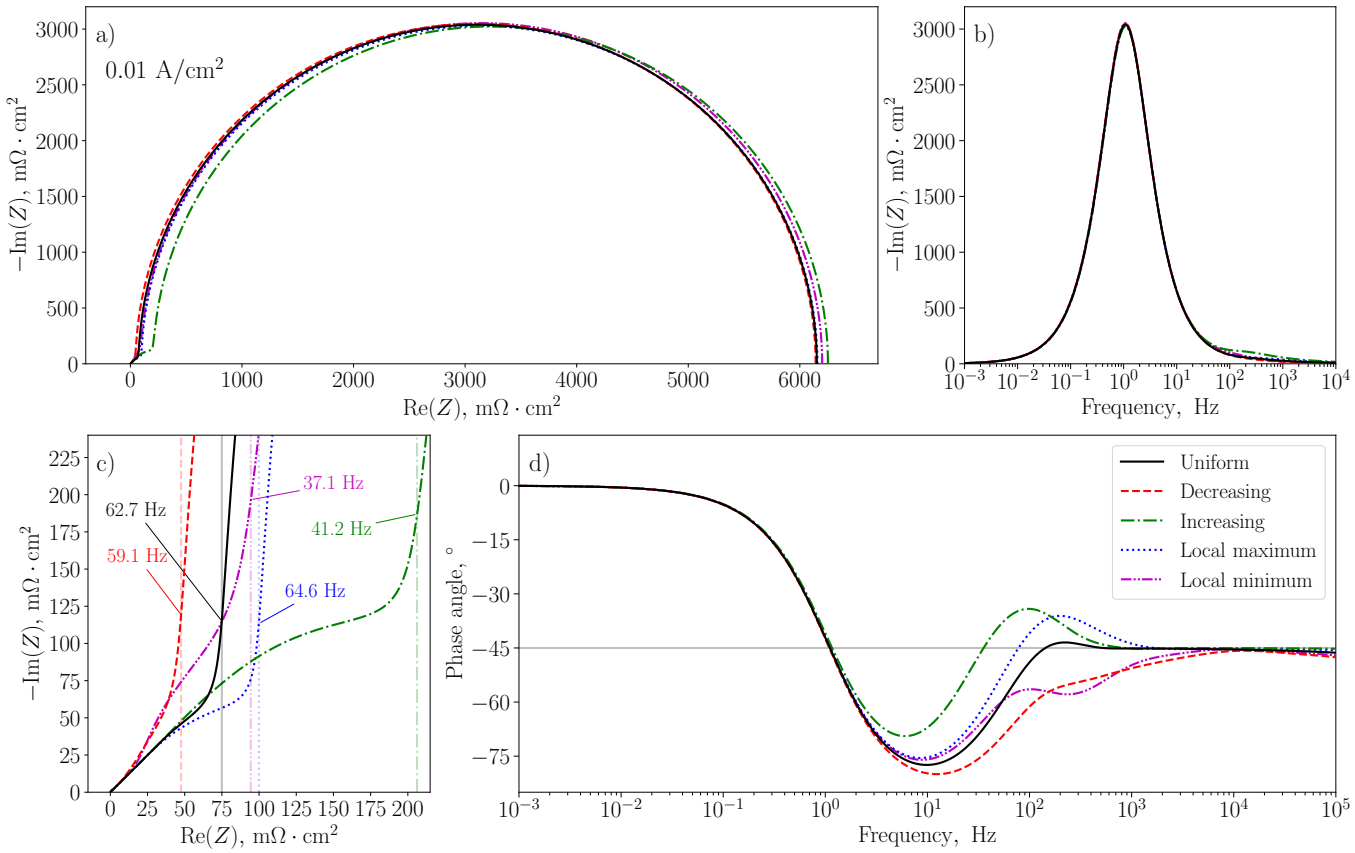

Figure 12: Comparison of the H_2/O_2 spectra simulated numerically for the ionomer-loading distributions from Figure 1 at 0.01 A/cm^2: a), c) Nyquist plot and its high-frequency portion; b), d) Bode plot of the imaginary impedance component and its high-frequency portion. Vertical lines represent the total ohmic resistance computed through ohmic heating (equations (6) and (7)).

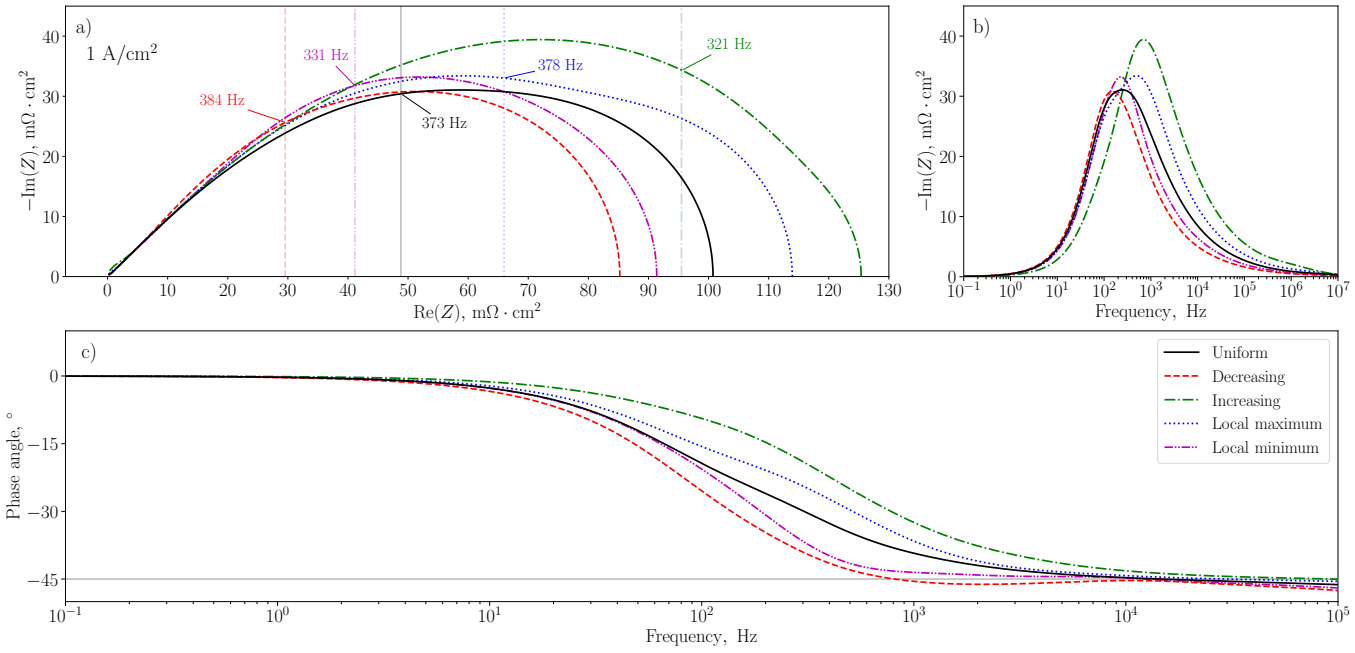

Figure 13: Comparison of the H_2/O_2 spectra simulated numerically for the ionomer-loading distributions from Figure 1 at 1 A/cm^2: a) Nyquist plot and b) Bode plot of the imaginary impedance component. Vertical lines represent the total ohmic resistance computed through ohmic heating (equations (6) and (7)).

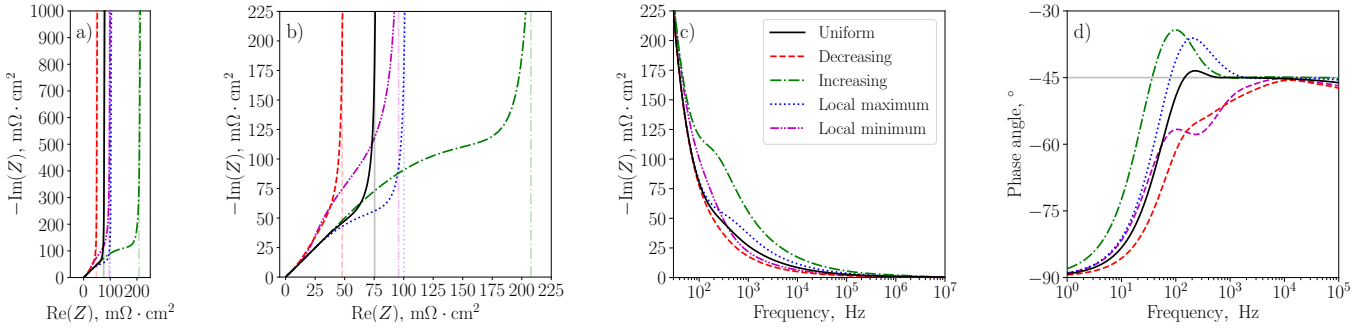

Figure 14: Comparison of the H_2/N_2 spectra simulated numerically for the ionomer-loading distributions from Figure 1: a), b) Nyquist plot and its high-frequency portion; c) Bode plot of the imaginary impedance component (high-frequency portion). Vertical lines represent the total ohmic resistance computed through ohmic heating (equations (6) and (7); estimates at 0.1 mA/cm^2 are shown).

4.4.3. H_2/N_2 spectroscopy

The H_2/N_2 spectra that correspond to the catalyst layers considered in the previous section are shown in Figure 14. Unlike the H_2/O_2 spectroscopy, H_2/N_2 EIS allows to unambiguously determine the total ohmic resistance of the catalyst layer from the position of the linear low-frequency impedance branch (at frequencies below 1–10 Hz), as seen in Figures 14(a) and (b). However, the protonic and electronic conductivities of a heterogeneous catalyst layer cannot be determined from the impedance spectrum as equation (21) does not hold even at the zero-current limit (Figure 10 and Table 7). Similar results were obtained for a catalyst layer with low electronic conductivity (based on case IV; shown in Figure S12 in the Supplementary Information).

4.5. Effect of heterogeneous active area and double-layer capacitance

The effect of catalyst distribution was analyzed in isolation from ionomer content by considering a graded catalyst layer with heterogeneous active area. In each of the five CL zones, A_v was scaled by the same factors as ionomer loading in the previous study. Because double-layer capacitance is related to active area, it was also scaled by the same factors. The active-area and capacitance distributions used in the simulations are shown in Figure S13 in the Supplementary Information. All other catalyst-layer properties were taken from the uniform case I.

The simulated ohmic resistance and impedance spectra exhibited trends similar to those in the ionomer-loading study (Figures S14–S16 in the Supplementary Information). Even though impedance was significantly less sensitive to the changes in active area and double-layer capacitance, it is clear that the spectrum distortion seen in Figures 12 and 14 is not indicative of the ionomer-loading distribution alone. Such an impedance distortion may also be caused by strong heterogeneity in active area (and double-layer capacitance). Therefore, no conclusions on catalyst-layer structure should be made from the shape of the impedance spectrum. Moreover, even small differences in the spectrum shape may indicate a noticeable change in the effective protonic and electronic resistances of the layer, as shown in Figures S14(a) and S14(b) in the Supplementary Information. Thus, the impedance relations for homogeneous catalyst layers from references [19,48,49] should not be used to analyze distorted spectra. Impedance-spectrum distortions should be interpreted with numerical models, as analytical expressions for heterogeneous CLs are often limited to a particular catalyst-layer-property distribution (see, for instance, references [55,76,77]).

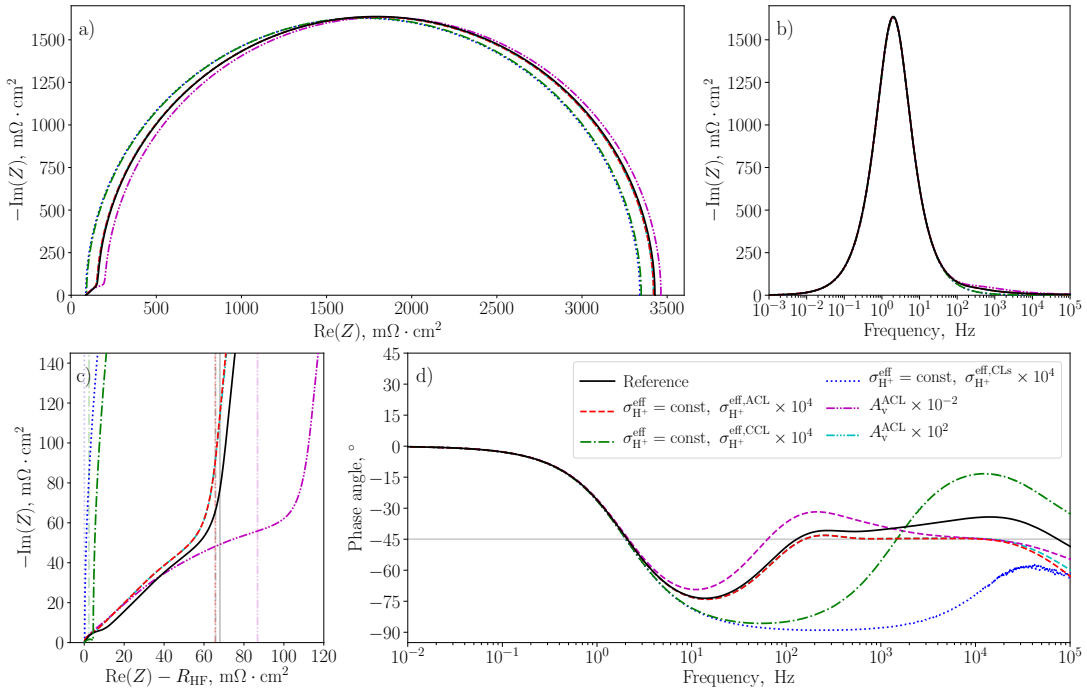

Figure 15: Comparison of the H_2/O_2 spectra simulated numerically at 0.01 A/cm^2 with the 2D PEMFC model from reference[62]: a), c) Nyquist plot and its high-frequency portion; b), d) Bode plot of the imaginary impedance component and its high-frequency portion. Vertical lines represent the total ohmic resistance of the ACL and the CCL computed through ohmic heating (equations (6) and (7)). Curves corresponding to the highly conductive ACL and the ACL with large active area coincide in the shown plots. Phase angle is reported for the HFR-corrected spectra.

4.6. Effect of anode catalyst layer on H_2/O_2 PEMFC impedance

Transient responses from anode and cathode catalyst layers may interfere with each other in physical experiments, where impedance spectra are measured for a whole electrochemical cell in contrast to a single catalyst layer. In order to analyze the effect of the anode catalyst layer on the fuel-cell H_2/O_2 EIS measurements, a parametric study was performed at 0.01 A/cm^2 using the 2D PEMFC model from reference[62] (Figure 15). The H_2/O_2 conditions were chosen over the H_2/N_2 conditions as the former allow for the rapid-EIS approach discussed in this work and in references[62,85]. As shown earlier, the two methods result in similar impedance spectra at high frequencies when H_2/O_2 EIS is performed at 0.01 A/cm^2.

In the reference case, two distinct arcs were observed, one between 100 Hz and 1 kHz and another at frequencies above 1 kHz (Figures 15(c) and (d)). In order to identify the nature of these arcs, protonic conductivities of the catalyst layers and the membrane were first made constant and uniform (independently in each layer). This had no effect on the impedance spectrum, as electrolyte hydration was relatively uniform at the given current density. Further modifications were made by increasing the protonic conductivity of first the ACL, then the CCL by a factor of 10^4. When the ACL was highly protonically conductive, the arc at frequencies above 1 kHz disappeared, revealing the linear 45° branch as seen in Figures 15(c) and (d). On the other hand, a high protonic conductivity of the CCL resulted in a spectrum with a capacitive arc at frequencies above 1 kHz but without the arc at frequencies between 100 Hz and 1 kHz. With high protonic conductivity of both catalyst layers, both arcs were negligible in size. Therefore, the arc at frequencies between 100 Hz and 1 kHz represents the CCL, and the arc at higher frequencies

is related to the ACL, where a faster (compared to the ORR) hydrogen oxidation reaction occurs.

The ACL effect on the PEMFC impedance spectrum was investigated further by modifying active area. Increasing the active area of the ACL by a factor of 10^2 revealed the 45° branch (Figures 15(c) and (d); that spectrum overlaps with the $\sigma_{H^+}^{\text{eff, ACL}} \times 10^4$ case). On the other hand, a significant spectrum distortion took place at frequencies above 5 Hz when the active area of the ACL was decreased by two orders of magnitude. Such a distortion was not a multidimensional effect, as the protonic potential was nearly uniform in the in-plane direction in the two catalyst layers and the membrane. Total ohmic resistance of the ACL and the CCL, computed through ohmic heating with equations (6) and (7), was smaller than the projection of the apparent high-frequency arc onto the real axis (Figure 15(c)), indicating a significant contribution of the faradaic ACL impedance. The same was observed when a highly protonically conductive CCL was used, but not in other cases. Therefore, in order for the PEMFC spectrum to contain the 45° branch that enables catalyst-layer charge-transport analysis with analytical models, both faradaic and ohmic effects of the ACL must be minimized. When the CCL charge-transport properties are to be analyzed, ACLs must be fabricated with sufficiently high catalyst and ionomer loading.

Equation (18) was fitted to the two spectra from Figure 15 that exhibited the 45° branch. Since these cases (high ACL protonic conductivity and active area) did not contain the anode effects, a single catalyst-layer impedance was used, as opposed to a sum of two impedance relations (18) representing a series connection of the ACL and the CCL. The spectra were corrected for the ohmic resistance of the membrane and the gas-diffusion layers (computed through ohmic heating) prior to the fitting. Residual of both fits was within 0.6 $\text{m}\Omega \cdot \text{cm}^2$, and R^2 was at least 0.999. The fitted protonic conductivity was 2.26 mS/cm for the case with high ACL protonic conductivity and 2.20 mS/cm for the case with high ACL active area. Both fitted conductivities were close to the exact average effective protonic conductivity of the CCL, 2.27 mS/cm. Effective electronic conductivity was fitted to be 1.34 S/cm in the case with a highly conductive ACL and could not be fitted in the case with a highly active ACL (a value of the order of 10^{14} S/cm was obtained) due to the low sensitivity of the CL impedance to the relatively high effective electronic conductivity (about 3.79 S/cm). This illustrates the applicability of equation (18) to estimating CCL proton-transport properties when a PEMFC spectrum is free of anodic effects. Electron-transport properties can also be extracted, as shown earlier, if electronic conductivity is not significantly higher than protonic conductivity.

5. Conclusions

A one-dimensional transient numerical model was used to generate impedance spectra of PEMFC and PEMWE catalyst layers with known electronic and protonic conductivity. The simulated spectra and the estimated ohmic-heating-based resistance were used to assess the validity of the analytical expressions proposed in the literature for estimating effective catalyst-layer charge-transport properties under a variety of conditions, such as multi-step kinetics, heterogeneous ionomer and active-area distributions, and strong anodic effects (a two-dimensional PEMFC model was used in the latter study).

Based on this work, the following recommendations can be given for the estimation of the catalyst-layer charge-transport properties via EIS. Under the H_2/O_2 operating conditions, equation (18) should be chosen over equation (16) for fitting as the former allows to simultaneously estimate the proton- and electron-transport properties and does not overestimate the ohmic resistance. Ohmic resistance and effective conductivity are related with equa-

tion (21). While the conductivity estimation is reasonably accurate at any current density (Table 5), a reliable ohmic-resistance measurement is only possible at low current densities confined by equation (22). If one of the catalyst-layer conductivities is known (for example, from a four-probe measurement [10,11]), the other one can be found from the HFR using equation (19) (after a correction for other cell components). Additionally, the ORR kinetic study performed in this work indicates that the catalyst-layer charge-transport characterization should only be performed at low current density and at sufficiently high frequencies to avoid the propagation of the faradaic effects to the frequencies of interest. If the order of magnitude of the catalyst-layer conductivities can be estimated, the required minimum frequency and the maximum applicable current density can be found from equations (32) and equation (33), respectively.

The H_2/N_2 spectroscopy is more commonly used in the literature for the charge-transport characterization as it allows for better control of the local relative humidity and temperature due to the absence of faradaic reactions in the working electrode. Equations (16) and (23) can be used to analyze the H_2/N_2 spectra, but equation (25) should be preferred as it has the same advantages as equation (18) in the H_2/O_2 case, e.g., the ability to estimate both electronic- and protonic-transport properties, which is important in case of PEMWE ACLs that may exhibit low electronic conductivity. If the vertical low-frequency branch is present in the measured H_2/N_2 spectrum, a simple graphical approach can be used to extract the protonic and electronic conductivities (Figure 3(b) and equations (28) and (29)). The respective ohmic resistances can then be accurately calculated with equation (21).

One of the downsides of equations (18), (25) and their limiting cases is the low sensitivity to the more conductive phase. If one of the conductivities is significantly higher than the other, the obtained charge-transport properties may not be as accurate as those for the less conductive phase (Tables 4 and 5). Moreover, two pairs of conductivities (and thus two pairs of ohmic resistances) satisfy the same impedance spectrum (equations (28) and (29)). Assignment of the extracted property to a given phase is not possible without knowing which phase is more conductive.

If the spectrum deviates from the ideal 45° line at high frequencies after the inductance correction (performed via either equivalent-circuit fitting [19,62] or short-circuit measurements [101]), the observed impedance may signify catalyst-layer inhomogeneity [16,21,22,38,55,57,63,76–78]. This inhomogeneity may be caused either by the structural properties of the layer, such as the ionomer and active-area distributions, or by the nonuniform hydration and degradation. Other hypothesized reasons include complex pore structure [16,38,57,58], nonuniform CL thickness [22,57], and additional double-layer capacitance of the ionomer-carbon and ionomer-water interfaces [56]. Even though analytical [55,56,77] and equivalent-circuit [22] models exist that account for some of the aforementioned factors, they either were designed for a specific type of inhomogeneity [22,55,77] and are not general, or represent a catalyst layer as a single pore [56], which is not accurate. Therefore, catalyst-layer conductivity cannot be reliably extracted from the spectrum with a distortion at frequencies between 10 Hz–10 kHz. However, total ohmic resistance can be estimated from H_2/N_2 measurements as long as the vertical impedance branch is observed at frequencies below 1–10 Hz (Figure 14).

Catalyst-layer heterogeneity has been hypothesized [16,20,28,35,42,63,78] to also induce a deviation from the low-frequency 90° slope in the H_2/N_2 spectra [10,12,16,20,22,25–30,32,34,35,37–39,42,47,63]. However, it has been shown in this work and in references [21,22] that the 90° branch is observed even in catalyst layers with nonuniform distributions of ionomer, active area, and double-layer capacitance. Therefore, the commonly observed distortion of the H_2/N_2 impedance at frequencies below 1–10 Hz is likely due to hydrogen crossover [20,21] or oxygen traces in the

cathode stream[38]. The resulting faradaic processes cannot be described with equations (23) and (25) or with the respective graphical methods, and equations (16) and (18) should be used instead.

It has been shown in this work that homogeneity of the catalyst layer in the working electrode is necessary but not sufficient for the spectrum to contain the 45° branch. Low catalyst loading and low conductivity of the reference electrode (e.g., ACL in PEMFCs) may also distort the spectrum and obstruct its analysis with analytical models.

Heterogeneity in ionomer loading, heterogeneity in active area, and strong effects of the reference electrode all lead to similar changes in the shape of the spectrum at frequencies above 5 Hz, and no conclusions on the working-electrode structure can be made. This highlights the importance of advanced mathematical modeling in the interpretation of experimental PEMFC and PEMWE impedance spectra.

Conflicts of interest

There are no conflicts to declare.

Acknowledgment

The authors thank Dr. Petar Minev (Department of Mathematical and Statistical Sciences, University of Alberta, Canada) for the mathematical guidance during the development of the transient framework in OpenFCST, Mr. Aidan Heaman (Department of Mechanical Engineering, University of Alberta, Canada) for the assistance at the early development stages of the EIS post-processing framework in OpenFCST, and Dr. Andrei Kulikovsky (Forschungszentrum Jülich, Germany) for the discussion of the derivation of equation (20). The authors acknowledge the Natural Sciences and Engineering Council of Canada (NSERC), CREATE-ME^2 (Collaborative Research and Training Experience Program - Materials for Electrochemical Energy Solutions Initiative, Canada), the Automotive Fuel Cell Cooperation Corporation (AFCC, Canada), and Johnson Matthey (UK) for their financial assistance.

Nomenclature

i	imaginary unit
A_v	volumetric active area, $\mathrm{cm}^2_\mathrm{cat}/\mathrm{cm}^3$
b	Tafel slope, V
C	volumetric capacitance, F/cm^3
c	concentration, $\mathrm{mol}/\mathrm{cm}^3$
C^*	areal capacitance, F/cm^2
D	diffusion coefficient, cm^2/s
E_th	theoretical half-cell potential, V

F Faraday constant, ≈96485 C/mol

i areal current density, $\mathrm{A/cm^2}$

i_0 areal exchange current density, $\mathrm{A/cm^2}$

j volumetric current density, $\mathrm{A/cm^3}$

L thickness of the catalyst layer, µm (unless otherwise stated)

R universal gas constant, ≈8.314 J/(mol K), or resistance, $\mathrm{m\Omega \cdot cm^2}$ (unless otherwise stated)

T temperature, K

t time, s

V voltage, V

x molar fraction

Z impedance, $\mathrm{m\Omega \cdot cm^2}$ (unless otherwise stated)

Greek letters

α charge-transfer coefficient

η overpotential, $\eta = \phi_{\mathrm{e^-}} - \phi_{\mathrm{H^+}} - E_{\mathrm{th}}$, V

ω angular frequency, rad/s

ϕ potential, V

σ electrical conductivity, S/cm

ε volume fraction

Subscripts and superscripts

Ω ohmic property

$\mathrm{e^-}$ electron

$\mathrm{H^+}$ hydrogen proton

$\mathrm{H_2}$ hydrogen

$\mathrm{N_2}$ nitrogen

$\mathrm{O_2}$ oxygen

0 property at the given operating conditions

ct charge transfer

ct+pe charge transfer, proton and electron transport

DC direct current

dl double layer

eff effective transport property

HF high frequency

ox oxygen transport

tot total

v void phase (pore)

Appendix A. Derivation of equation (11) from equation (2)

Consider a problem of one-dimensional proton transport in a cathode catalyst layer with fast oxygen and electron transport. Under the assumption of Tafel kinetics (equation (4)) and constant protonic conductivity, equation (2) is transformed into

$$-C_{\mathrm{dl}}\frac{\partial \eta}{\partial t} - \sigma^{\mathrm{eff}}_{\mathrm{H^+}}\frac{\partial^2 \phi_{\mathrm{H^+}}}{\partial x^2} = -\xi \exp\left(-\frac{\eta}{b}\right), \tag{A.1}$$

where we denote $\xi = i_0 A_{\mathrm{v}} \left(c^{\mathrm{cat|i}}_{\mathrm{O_2}}/c^{\mathrm{ref}}_{\mathrm{O_2}}\right)^{\gamma}$ for convenience. Based on the definition of the overpotential ($\eta = \phi_{\mathrm{e^-}} - \phi_{\mathrm{H^+}} - E_{\mathrm{th}}$) and the assumption that the layer is highly electronically conductive, $\phi_{\mathrm{H^+}}$ can be replaced with $-\eta$ under the spatial derivative in equation (A.1) (the theoretical half-cell potential E_{th} is independent of t and x in the considered case). When overpotential η is small, the exponent in equation (A.1) can be linearized to give

$$-C_{\mathrm{dl}}\frac{\partial \eta}{\partial t} + \sigma^{\mathrm{eff}}_{\mathrm{H^+}}\frac{\partial^2 \eta}{\partial x^2} = -\xi \left(1 - \frac{\eta}{b}\right), \tag{A.2}$$

where $\xi = i_0 A_{\mathrm{v}}$ due to negligible mass-transport limitations.

Let us represent the applied harmonic perturbation in the overpotential as

$$\eta(t, x, \omega) = \bar{\eta}(x) + \tilde{\eta}(x, \omega)\exp(\mathrm{i}\omega t). \tag{A.3}$$

Substituting equation (A.3) into equation (A.2) and noting that $\bar{\eta}(x)$ is the steady-state solution of the latter, one gets

$$\frac{\partial^2 \tilde{\eta}}{\partial x^2}\exp(\mathrm{i}\omega t) = \frac{\tilde{\eta}}{\sigma^{\mathrm{eff}}_{\mathrm{H^+}}}\left(\frac{\xi}{b} + \mathrm{i}\omega C_{\mathrm{dl}}\right)\exp(\mathrm{i}\omega t). \tag{A.4}$$

Equation (A.4) must hold for all t and ω, and thus the following ordinary differential equation for the perturbation $\tilde{\eta}(x, \omega)$ is obtained:

$$\frac{\partial^2 \tilde{\eta}}{\partial x^2} = \frac{\tilde{\eta}}{\sigma^{\mathrm{eff}}_{\mathrm{H^+}}}\left(\frac{\xi}{b} + \mathrm{i}\omega C_{\mathrm{dl}}\right). \tag{A.5}$$

Because only protonic transport is considered, perturbation $\tilde{\eta}(x, \omega)$ is driven through the proton-exchange membrane of the cell. Thus, a boundary condition

$$\tilde{\eta}(0, \omega) = \tilde{\eta}^0(\omega) \tag{A.6}$$

is imposed at the CL-PEM interface ($x = 0$). Since the gas-diffusion layer is not protonically conductive, $-\sigma^{\text{eff}}_{\text{H}^+}\partial\phi_{\text{H}^+}/\partial x = 0$ must be satisfied at the CL-PTL interface ($x = L$). This is equivalent to setting

$$\frac{\partial\bar{\eta}}{\partial x}(L) + \frac{\partial\tilde{\eta}}{\partial x}(L,\omega)\exp(\mathrm{i}\omega t) = 0. \tag{A.7}$$

Protonic flux through the CL-PTL boundary must be zero at steady state as well, and thus $\partial\bar{\eta}/\partial x = 0$ at $x = L$. Therefore, the second term of equation (A.7) must be zero for all t and ω, from where it follows that

$$\frac{\partial\tilde{\eta}}{\partial x}(L,\omega) = 0. \tag{A.8}$$

We will search for the solution to equation (A.5) in the form [99]

$$\tilde{\eta}(x,\omega) = A(\omega)\exp\left((L-x)\tilde{Z}(\omega)\right) + B(\omega)\exp\left(-(L-x)\tilde{Z}(\omega)\right), \tag{A.9}$$

where

$$\tilde{Z}(\omega) = \sqrt{\frac{1}{\sigma^{\text{eff}}_{\text{H}^+}}\left(\frac{\xi}{b} + \mathrm{i}\omega C_{\text{dl}}\right)}. \tag{A.10}$$

Substitution of equation (A.9) into the boundary conditions (A.6) and (A.8) gives

$$A(\omega) = B(\omega) = \frac{\tilde{\eta}^0(\omega)}{\exp\left(L\tilde{Z}\right) + \exp\left(-L\tilde{Z}\right)}, \tag{A.11}$$

although having $A(\omega) = B(\omega)$ is sufficient to derive the impedance.

The volumetric protonic current density (A/cm^3) is defined as

$$j_{\text{H}^+} = -\sigma^{\text{eff}}_{\text{H}^+}\frac{\partial^2\phi_{\text{H}^+}}{\partial x^2} = \sigma^{\text{eff}}_{\text{H}^+}\frac{\partial^2\eta}{\partial x^2},$$

and thus

$$\tilde{j}_{\text{H}^+}(x,\omega) = \sigma^{\text{eff}}_{\text{H}^+}\frac{\partial^2\tilde{\eta}}{\partial x^2}(x,\omega) = \sigma^{\text{eff}}_{\text{H}^+}\tilde{Z}^2(\omega)\tilde{\eta}(x,\omega). \tag{A.12}$$

Integration of equation (A.12) from $x = 0$ to $x = L$ results in the current-density perturbation (A/cm^2)

$$\tilde{i}_{\text{H}^+}(\omega) = \sigma^{\text{eff}}_{\text{H}^+}\tilde{Z}(\omega)A(\omega)\left(\exp\left(L\tilde{Z}\right) - \exp\left(-L\tilde{Z}\right)\right).$$

Impedance ($\Omega\cdot$cm^2) is computed as

$$Z(\omega) = \frac{\tilde{\eta}(0,\omega)}{\tilde{i}_{\text{H}^+}(\omega)} = \frac{\tilde{\eta}^0(\omega)}{\tilde{i}_{\text{H}^+}(\omega)} = \frac{1}{\sigma^{\text{eff}}_{\text{H}^+}\tilde{Z}(\omega)}\coth\left(L\tilde{Z}(\omega)\right). \tag{A.13}$$

Rearranging equation (A.13), we obtain

$$Z(\omega) = \sqrt{R_{\text{H}^+}Z_{\text{int}}(\omega)}\coth\left(\sqrt{\frac{R_{\text{H}^+}}{Z_{\text{int}}(\omega)}}\right),$$

where $Z_{\text{int}}(\omega)$ and R_{H^+} are defined in equations (12) and (14), respectively, and

$$R_{\text{ct}} = \frac{b}{\xi L}, \quad C^*_{\text{dl}} = C_{\text{dl}}L. \tag{A.14}$$

As discussed in the main text, equation (14) cannot be used to obtain the effective protonic resistance; it is used here to illustrate the similarity of equations (A.13) and (11) only. Note that the charge-transfer resistance defined in equation (A.14) was obtained with the assumption of small overpotential (small operating current). It is equivalent to the charge-transfer resistance computed directly from the Tafel kinetics (4),

$$R^{\text{Tafel}}_{\text{ct}} = \frac{\partial\eta}{\partial i} = -\frac{b}{i},$$

when $\eta = 0$. The negative sign in the equation above is due to i being the protonic current density in this derivation.

References

[1] D. Banham, S. Ye, Current status and future development of catalyst materials and catalyst layers for proton exchange membrane fuel cells: an industrial perspective, ACS Energy Letters 2 (3) (2017) 629–638.

[2] H. A. Gasteiger, S. S. Kocha, B. Sompalli, F. T. Wagner, Activity benchmarks and requirements for Pt, Pt-alloy, and non-Pt oxygen reduction catalysts for PEMFCs, Applied Catalysis B: Environmental 56 (1-2) (2005) 9–35.

[3] M. Mandal, A. Valls, N. Gangnus, M. Secanell, Analysis of inkjet printed catalyst coated membranes for polymer electrolyte electrolyzers, Journal of The Electrochemical Society 165 (7) (2018) F543–F552.

[4] T. Schuler, J. M. Ciccone, B. Krentscher, F. Marone, C. Peter, T. J. Schmidt, F. N. Büchi, Hierarchically structured porous transport layers for polymer electrolyte water electrolysis, Advanced Energy Materials 10 (2) (2020) 1903216.

[5] M. Bernt, A. Siebel, H. A. Gasteiger, Analysis of voltage losses in PEM water electrolyzers with low platinum group metal loadings, Journal of the Electrochemical Society 165 (5) (2018) F305.

[6] C. Rozain, E. Mayousse, N. Guillet, P. Millet, Influence of iridium oxide loadings on the performance of PEM water electrolysis cells: Part I–Pure IrO2-based anodes, Applied Catalysis B: Environmental 182 (2016) 153–160.

[7] C. Rozain, E. Mayousse, N. Guillet, P. Millet, Influence of iridium oxide loadings on the performance of PEM water electrolysis cells: Part II–Advanced oxygen electrodes, Applied Catalysis B: Environmental 182 (2016) 123–131.

[8] A. Kusoglu, A. Z. Weber, New insights into perfluorinated sulfonic-acid ionomers, Chemical reviews 117 (3) (2017) 987–1104.

[9] K. Karan, Interesting facets of surface, interfacial, and bulk characteristics of perfluorinated ionomer films, Langmuir (2019).

[10] T. Suzuki, H. Murata, T. Hatanaka, Y. Morimoto, Analysis of the catalyst layer of polymer electrolyte fuel cells, R&D Review of Toyota CRDL 39 (3) (2003).

[11] D. R. Morris, S. P. Liu, D. Villegas Gonzalez, J. T. Gostick, Effect of water sorption on the electronic conductivity of porous polymer electrolyte membrane fuel cell catalyst layers, ACS Applied Materials & Interfaces 6 (21) (2014) 18609–18618.

[12] A. Krasnova, N. Glebova, A. Nechitailov, A. Tomasov, N. Zelenina, Charge transfer in hydrogen fuel cell electrode containing carbon nanofibers, International Scientific Journal for Alternative Energy and Ecology (19-21) (2018) 40–51, (in Russian).

[13] M. Secanell, B. Carnes, A. Suleman, N. Djilali, Numerical optimization of proton exchange membrane fuel cell cathodes, Electrochimica Acta 52 (7) (2007) 2668–2682.

[14] D. Song, Q. Wang, Z. Liu, T. Navessin, M. Eikerling, S. Holdcroft, Numerical optimization study of the catalyst layer of PEM fuel cell cathode, Journal of Power Sources 126 (1-2) (2004) 104–111.

[15] G. Sasikumar, J. Ihm, H. Ryu, Optimum nafion content in PEM fuel cell electrodes, Electrochimica Acta 50 (2-3) (2004) 601–605.

[16] U. Babic, E. Nilsson, A. Pătru, T. J. Schmidt, L. Gubler, Proton transport in catalyst layers of a polymer electrolyte water electrolyzer: Effect of the anode catalyst loading, Journal of The Electrochemical Society 166 (4) (2019) F214.

[17] M. Mandal, M. Moore, M. Secanell, Measurement of the proton and electron conductivities of the pem water electrolyzer electrodes, ACS Applied Materials & Interfaces (Submitted).

[18] J. Hou, W. Song, H. Yu, Y. Fu, L. Hao, Z. Shao, B. Yi, Ionic resistance of the catalyst layer after the PEM fuel cell suffered freeze, Journal of Power Sources 176 (1) (2008) 118–121.

[19] R. Makharia, M. Mathias, D. Baker, Measurement of catalyst layer electrolyte resistance in PEFCs using electrochemical impedance spectroscopy, Journal of The Electrochemical Society 152 (5) (2005) A970–A977.

[20] M. Cimenti, D. Bessarabov, M. Tam, J. Stumper, Investigation of proton transport in the catalyst layer of PEM fuel cells by electrochemical impedance spectroscopy, ECS transactions 28 (23) (2010) 147–157.

[21] D. Malevich, B. R. Jayasankar, E. Halliop, J. G. Pharoah, B. A. Peppley, K. Karan, On the determination of PEM fuel cell catalyst layer resistance from impedance measurement in H2/N2 cells, Journal of the Electrochemical Society 159 (12) (2012) F888–F895.

[22] T. Gaumont, G. Maranzana, O. Lottin, J. Dillet, S. Didierjean, J. Pauchet, L. Guétaz, Measurement of protonic resistance of catalyst layers as a tool for degradation monitoring, International Journal of Hydrogen Energy 42 (3) (2017) 1800–1812.

[23] A. Young, J. Stumper, E. Gyenge, Characterizing the structural degradation in a PEMFC cathode catalyst layer: carbon corrosion, Journal of The Electrochemical Society 156 (8) (2009) B913–B922.

[24] J. W. Lim, Y.-H. Cho, M. Ahn, D. Y. Chung, Y.-H. Cho, N. Jung, Y. S. Kang, O.-H. Kim, M. J. Lee, M. Kim, et al., Ionic resistance of a cathode catalyst layer with various thicknesses by electrochemical impedance spectroscopy for PEMFC, Journal of The Electrochemical Society 159 (4) (2012) B378–B384.

[25] Z. Xie, T. Navessin, K. Shi, R. Chow, Q. Wang, D. Song, B. Andreaus, M. Eikerling, Z. Liu, S. Holdcroft, Functionally graded cathode catalyst layers for polymer electrolyte fuel cells II. Experimental study of the effect of nafion distribution, Journal of the Electrochemical Society 152 (6) (2005) A1171–A1179.

[26] Z. Xie, X. Zhao, M. Adachi, Z. Shi, T. Mashio, A. Ohma, K. Shinohara, S. Holdcroft, T. Navessin, Fuel cell cathode catalyst layers from "green" catalyst inks, Energy & Environmental Science 1 (1) (2008) 184–193.

[27] Q. Xue, D. jun Yang, B. Li, P. wen Ming, C. man Zhang, Quantitative analysis effect of the cathode catalyst layer with various ionomer ratio on PEMFC by protonic resistance, ECS Transactions 89 (7) (2019) 23.

[28] K. Talukdar, S. Helmly, M. Schulze, D. G. Sanchez, M. Handl, R. Hiesgen, J. Kraut, K. A. Friedrich, Enveloping of catalyst powder by ionomer for dry spray coating in polymer electrolyte membrane fuel cells, Journal of Power Sources 424 (2019) 82–90.

[29] S. Vierrath, M. Breitwieser, M. Klingele, B. Britton, S. Holdcroft, R. Zengerle, S. Thiele, The reasons for the high power density of fuel cells fabricated with directly deposited membranes, Journal of Power Sources 326 (2016) 170–175.

[30] S. Shukla, Experimental analysis of inkjet printed polymer electrolyte fuel cell electrodes, Ph.D. thesis, University of Alberta (2016).

[31] S. Shukla, D. Stanier, M. Saha, J. Stumper, M. Secanell, Analysis of inkjet printed PEFC electrodes with varying platinum loading, Journal of The Electrochemical Society 163 (7) (2016) F677–F687.

[32] S. Shukla, K. Domican, K. Karan, S. Bhattacharjee, M. Secanell, Analysis of low platinum loading thin polymer electrolyte fuel cell electrodes prepared by inkjet printing, Electrochimica Acta 156 (2015) 289–300.

[33] S. Shukla, D. Stanier, M. S. Saha, B. Zahiri, M. Tam, J. Stumper, M. Secanell, Characterization of inkjet printed electrodes with improved porosity, ECS Transactions 77 (11) (2017) 1453.

[34] Y. Garsany, R. W. Atkinson, M. B. Sassin, R. M. Hjelm, B. D. Gould, K. E. Swider-Lyons, Improving pemfc performance using short-side-chain low-equivalent-weight PFSA ionomer in the cathode catalyst layer, Journal of The Electrochemical Society 165 (5) (2018) F381–F391.

[35] A. D. Modestov, A. V. Kapustin, V. B. Avakov, I. K. Landgraf, M. R. Tarasevich, Cathode catalyst layers with ionomer to carbon mass ratios in the range 0–2 studied by electrochemical impedance spectroscopy, cyclic voltammetry, and performance measurements, Journal of Power Sources 272 (2014) 735–742.

[36] T. Soboleva, K. Malek, Z. Xie, T. Navessin, S. Holdcroft, PEMFC catalyst layers: the role of micropores and mesopores on water sorption and fuel cell activity, ACS Applied Materials & Interfaces 3 (6) (2011) 1827–1837.

[37] M. Darab, A. O. Barnett, G. Lindbergh, M. S. Thomassen, S. Sunde, The influence of catalyst layer thickness on the performance and degradation of PEM fuel cell cathodes with constant catalyst loading, Electrochimica Acta 232 (2017) 505–516.

[38] J. Gazzarri, M. Eikerling, Q. Wang, Z.-S. Liu, Estimation of local relative humidity in cathode catalyst layers of PEFC, Electrochemical and Solid-State Letters 13 (6) (2010) B58–B62.

[39] B. P. Setzler, T. F. Fuller, A physics-based impedance model of proton exchange membrane fuel cells exhibiting low-frequency inductive loops, Journal of The Electrochemical Society 162 (6) (2015) F519–F530.

[40] J. Peron, D. Edwards, M. Haldane, X. Luo, Y. Zhang, S. Holdcroft, Z. Shi, Fuel cell catalyst layers containing short-side-chain perfluorosulfonic acid ionomers, Journal of Power Sources 196 (1) (2011) 179–181.

[41] M. S. Kondratenko, M. O. Gallyamov, A. R. Khokhlov, Performance of high temperature fuel cells with different types of PBI membranes as analysed by impedance spectroscopy, International Journal of Hydrogen Energy 37 (3) (2012) 2596–2602.

[42] M.-J. Choo, K.-H. Oh, H.-T. Kim, J.-K. Park, Modulated ionomer distribution in the catalyst layer of polymer electrolyte membrane fuel cells for high temperature operation, ChemSusChem 7 (8) (2014) 2335–2341.

[43] X. Zhao, X. Fan, S. Wang, S. Yang, B. Yi, Q. Xin, G. Sun, Determination of ionic resistance and optimal composition in the anodic catalyst layers of DMFC using AC impedance, International journal of hydrogen energy 30 (9) (2005) 1003–1010.

[44] A. Havranek, K. Wippermann, Determination of proton conductivity in anode catalyst layers of the direct methanol fuel cell (DMFC), Journal of Electroanalytical Chemistry 567 (2) (2004) 305–315.

[45] S. Tominaka, K. Goto, T. Momma, T. Osaka, Ionic conductivity improvement in primary pores of fuel cell catalyst layers: Electropolymerization of m-aminobenzenesulfonic acid and its effect on the performance, Journal of Power Sources 192 (2) (2009) 316–323.

[46] K. Cooper, V. Ramani, J. M. Fenton, H. Kunz, Experimental methods and data analyses for polymer electrolyte fuel cells, Scribner Associates, Inc., Illinois, 2009.

[47] U. Babic, T. J. Schmidt, L. Gubler, Communication—Contribution of catalyst layer proton transport resistance to voltage loss in polymer electrolyte water electrolyzers, Journal of The Electrochemical Society 165 (15) (2018) J3016–J3018.

[48] M. Eikerling, A. Kornyshev, Electrochemical impedance of the cathode catalyst layer in polymer electrolyte fuel cells, Journal of Electroanalytical Chemistry 475 (2) (1999) 107–123.

[49] A. Kulikovsky, A model for impedance of a pem fuel cell cathode with poor electron conductivity, Journal of Electroanalytical Chemistry 801 (2017) 122–128.

[50] J. X. Wang, F. A. Uribe, T. E. Springer, J. Zhang, R. R. Adzic, Intrinsic kinetic equation for oxygen reduction reaction in acidic media: the double Tafel slope and fuel cell applications, Faraday discussions 140 (2009) 347–362.

[51] M. Moore, Investigation of the dobule-trap intrinsic kinetic equation for oxygen reduction reaction and its implementation into a membrane electrode assembly model, Master's thesis, University of Alberta (2012).

[52] M. Moore, A. Putz, M. Secanell, Investigation of the orr using the double-trap intrinsic kinetic model, Journal of the Electrochemical Society 160 (6) (2013) F670–F681.

[53] J. Wu, L. G. Melo, X. Zhu, M. M. West, V. Berejnov, D. Susac, J. Stumper, A. P. Hitchcock, 4D imaging of polymer electrolyte membrane fuel cell catalyst layers by soft X-ray spectro-tomography, Journal of Power Sources 381 (2018) 72–83.

[54] J. Jankovic, S. Zhang, A. Putz, M. S. Saha, D. Susac, Multi-scale imaging and transport modeling for fuel cell electrode, J Mater Res, 2017 MRS Fall Focus Issue 34 (2019).

[55] A. Kulikovsky, Impedance of a PEM fuel cell cathode with nonuniform ionomer loading: Analytical and numerical study, Journal of Electroanalytical Chemistry 789 (2017) 174–180.

[56] T. Reshetenko, A. Kulikovsky, On the origin of high frequency impedance feature in a PEM fuel cell, Journal of The Electrochemical Society 166 (15) (2019) F1253–F1257.

[57] F. Jaouen, G. Lindbergh, K. Wiezell, Transient techniques for investigating mass-transport limitations in gas diffusion electrodes ii. experimental characterization of the PEFC cathode, Journal of The Electrochemical Society 150 (12) (2003) A1711–A1717.

[58] D. Malko, T. Lopes, E. A. Ticianelli, A. Kucernak, A catalyst layer optimisation approach using electrochemical impedance spectroscopy for PEM fuel cells operated with pyrolysed transition metal-NC catalysts, Journal of Power Sources 323 (2016) 189–200.

[59] G. A. Futter, P. Gazdzicki, K. A. Friedrich, A. Latz, T. Jahnke, Physical modeling of polymer-electrolyte membrane fuel cells: Understanding water management and impedance spectra, Journal of Power Sources 391 (2018) 148–161.

[60] T. Reshetenko, A. Kulikovsky, Comparison of two physical models for fitting PEM fuel cell impedance spectra measured at a low air flow stoichiometry, Journal of The Electrochemical Society 163 (3) (2016) F238–F246.

[61] T. Romero-Castanon, L. Arriaga, U. Cano-Castillo, Impedance spectroscopy as a tool in the evaluation of MEA's, Journal of power sources 118 (1-2) (2003) 179–182.

[62] A. Kosakian, L. Padilla Urbina, A. Heaman, M. Secanell, Understanding single-phase water-management signatures in fuel-cell impedance spectra: A numerical study, Electrochimica Acta 350 (2020) 136204.

[63] M. C. Lefebvre, R. B. Martin, P. G. Pickup, Characterization of ionic conductivity profiles within proton exchange membrane fuel cell gas diffusion electrodes by impedance spectroscopy, Electrochemical and Solid State Letters 2 (6) (1999) 259.

[64] P. Moçotéguy, B. Ludwig, D. Beretta, T. Pedersen, Study of the impact of water management on the performance of pemfc commercial stacks by impedance spectroscopy, International Journal of Hydrogen Energy(in press) (2020).

[65] V. Paganin, C. Oliveira, E. Ticianelli, T. Springer, E. Gonzalez, Modelistic interpretation of the impedance response of a polymer electrolyte fuel cell, Electrochimica Acta 43 (24) (1998) 3761–3766.

[66] S. J. Andreasen, J. L. Jespersen, E. Schaltz, S. K. Kær, Characterisation and modelling of a high temperature PEM fuel cell stack using electrochemical impedance spectroscopy, Fuel Cells 9 (4) (2009) 463–473.

[67] F. J. Pinar, N. Pilinski, M. Rastedt, P. Wagner, Performance of a high-temperature PEM fuel cell operated with oxygen enriched cathode air and hydrogen from synthetic reformate, International Journal of Hydrogen Energy 40 (15) (2015) 5432–5438.

[68] T. Reshetenko, A. Kulikovsky, PEM fuel cell characterization by means of the physical model for impedance spectra, Journal of The Electrochemical Society 162 (7) (2015) F627.

[69] M. Secanell, A. Putz, S. Shukla, P. Wardlaw, M. Bhaiya, L. M. Pant, M. Sabharwal, Mathematical Modelling and Experimental Analysis of Thin, Low-Loading Fuel Cell Electrodes, ECS Transactions 69 (17) (2015) 157–187.

[70] J. Zhou, D. Stanier, A. Putz, M. Secanell, A mixed wettability pore size distribution based mathematical model for analyzing two-phase flow in porous electrodes II. Model validation and analysis of micro-structural parameters, Journal of The Electrochemical Society 164 (6) (2017) F540–F556.

[71] M. Secanell, Computational modeling and optimization of proton exchange membrane fuel cells, Ph.D. thesis, University of Victoria (2007).

[72] A. Parthasarathy, S. Srinivasan, A. J. Appleby, C. R. Martin, Temperature dependence of the electrode kinetics of oxygen reduction at the platinum/nafion® interface - A microelectrode investigation, Journal of the Electrochemical Society 139 (9) (1992) 2530–2537.

[73] A. Parthasarathy, S. Srinivasan, A. J. Appleby, C. R. Martin, Pressure dependence of the oxygen reduction reaction at the platinum microelectrode/Nafion interface: Electrode kinetics and mass transport, Journal of the Electrochemical Society 139 (10) (1992) 2856–2862.

[74] W. Sun, B. A. Peppley, K. Karan, An improved two-dimensional agglomerate cathode model to study the influence of catalyst layer structural parameters, Electrochimica acta 50 (16-17) (2005) 3359–3374.

[75] M. Moore, P. Wardlaw, P. Dobson, J. Boisvert, A. Putz, R. Spiteri, M. Secanell, Understanding the effect of kinetic and mass transport processes in cathode agglomerates, Journal of the Electrochemical Society 161 (8) (2014) E3125–E3137.

[76] D. Gerteisen, Impact of inhomogeneous catalyst layer properties on impedance spectra of polymer electrolyte membrane fuel cells, Journal of The Electrochemical Society 162 (14) (2015) F1431–F1438.

[77] T. Reshetenko, A. Kulikovsky, Impedance spectroscopy study of the PEM fuel cell cathode with nonuniform Nafion loading, Journal of The Electrochemical Society 164 (11) (2017) E3016–E3021.

[78] G. Li, P. G. Pickup, Ionic conductivity of PEMFC electrodes effect of Nafion loading, Journal of The Electrochemical Society 150 (11) (2003) C745–C752.

[79] M. Secanell, A. Putz, P. Wardlaw, V. Zingan, M. Bhaiya, M. Moore, J. Zhou, C. Balen, K. Domican, OpenFCST: An open-source mathematical modelling software for polymer electrolyte fuel cells, ECS Transactions 64 (3) (2014) 655–680.

[80] OpenFCST: Open-Source Fuel Cell Simulation Toolbox (official website), `www.openfcst.org`, accessed on November 10, 2019.

[81] W. Bangerth, R. Hartmann, G. Kanschat, deal.II – A general-purpose object-oriented finite element library, ACM Transactions on Mathematical Software (TOMS) 33 (4) (2007) 24.

[82] W. Bangerth, D. Davydov, T. Heister, L. Heltai, G. Kanschat, M. Kronbichler, M. Maier, B. Turcksin, D. Wells, The deal.II library, version 8.4, Journal of Numerical Mathematics 24 (3) (2016) 135–141.

[83] I. Faragó, Á. Havasi, Z. Zlatev, Efficient implementation of stable richardson extrapolation algorithms, Computers & Mathematics with Applications 60 (8) (2010) 2309–2325.

[84] E. Hairer, S. P. Nørsett, G. Wanner, Solving Ordinary Differential Equations I: Nonstiff Problems, Springer Series in Computational Mathematics, Springer, 1993.

[85] W. G. Bessler, Rapid impedance modeling via potential step and current relaxation simulations, Journal of The Electrochemical Society 154 (11) (2007) B1186–B1191.

[86] H. Wiese, K. G. Weil, An efficient fourier transform algorithm for frequency domains of several decades using logarithmically spaced time samples, IEEE Transactions on Acoustics, Speech, and Signal Processing 36 (7) (1988) 1096–1099.

[87] W. H. Press, S. A. Teukolsky, W. T. Vetterling, B. P. Flannery, Numerical recipes: The art of scientific computing, 3rd Edition, Cambridge University Press, 2007.

[88] P. Virtanen, R. Gommers, T. E. Oliphant, M. Haberland, T. Reddy, D. Cournapeau, E. Burovski, P. Peterson, W. Weckesser, J. Bright, et al., SciPy 1.0: fundamental algorithms for scientific computing in Python, Nature methods 17 (3) (2020) 261–272.

[89] I. Nitta, T. Hottinen, O. Himanen, M. Mikkola, Inhomogeneous compression of PEMFC gas diffusion layer: Part I. Experimental, Journal of Power Sources 171 (1) (2007) 26–36.

[90] H. Sadeghifar, In-plane and through-plane electrical conductivities and contact resistances of a Mercedes-Benz catalyst-coated membrane, gas diffusion and micro-porous layers and a Ballard graphite bipolar plate: Impact of humidity, compressive load and polytetrafluoroethylene, Energy Conversion and Management 154 (2017) 191–202.

[91] J. Kleemann, F. Finsterwalder, W. Tillmetz, Characterisation of mechanical behaviour and coupled electrical properties of polymer electrolyte membrane fuel cell gas diffusion layers, Journal of Power Sources 190 (1) (2009) 92–102.

[92] M. Ismail, T. Damjanovic, D. Ingham, M. Pourkashanian, A. Westwood, Effect of polytetrafluoroethylene-treatment and microporous layer-coating on the electrical conductivity of gas diffusion layers used in proton exchange membrane fuel cells, Journal of Power Sources 195 (9) (2010) 2700–2708.

[93] D. R. Morris, J. T. Gostick, Determination of the in-plane components of the electrical conductivity tensor in PEM fuel cell gas diffusion layers, Electrochimica acta 85 (2012) 665–673.

[94] R. De Levie, On porous electrodes in electrolyte solutions—IV, Electrochimica Acta 9 (9) (1964) 1231–1245.

[95] S. Cruz-Manzo, R. Chen, A generic electrical circuit for performance analysis of the fuel cell cathode catalyst layer through electrochemical impedance spectroscopy, Journal of Electroanalytical Chemistry 694 (2013) 45–55.

[96] M. Lefebvre, Z. Qi, D. Rana, P. G. Pickup, Chemical synthesis, characterization, and electrochemical studies of poly (3, 4-ethylenedioxythiophene)/poly (styrene-4-sulfonate) composites, Chemistry of materials 11 (2) (1999) 262–268.

[97] T. Reshetenko, A. Serov, M. Odgaard, G. Randolf, L. Osmieri, A. Kulikovsky, Electron and proton conductivity of Fe-NC cathodes for PEM fuel cells: A model-based electrochemical impedance spectroscopy measurement, Electrochemistry Communications (2020) 106795.

[98] S. M. R. Niya, M. Hoorfar, Study of proton exchange membrane fuel cells using electrochemical impedance spectroscopy technique–A review, Journal of Power Sources 240 (2013) 281–293.

[99] M. E. Orazem, B. Tribollet, Electrochemical impedance spectroscopy, 2nd Edition, John Wiley & Sons, 2017.

[100] X.-Z. Yuan, C. Song, H. Wang, J. Zhang, Electrochemical impedance spectroscopy in PEM fuel cells: fundamentals and applications, Springer Science & Business Media, 2009.

[101] T. Soboleva, Z. Xie, Z. Shi, E. Tsang, T. Navessin, S. Holdcroft, Investigation of the through-plane impedance technique for evaluation of anisotropy of proton conducting polymer membranes, Journal of Electroanalytical Chemistry 622 (2) (2008) 145–152.